

# **Engineering an Interfacial Facet of S-Scheme Heterojunction Ternary Nanocomposite for Enhanced Photocatalytic Activity**



**Name: Mah Roosh  
Reg No. 00000331027**

**A thesis submitted in partial fulfillment of the requirements for the degree  
of Master of Science in Chemistry**

**Supervised by: Dr. Shahid Iqbal**

**Department of Chemistry**

**School of Natural Sciences (SNS)**


**National University of Sciences and Technology (NUST)**

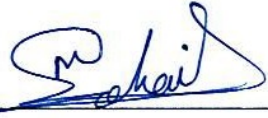
**H-12, Islamabad, Pakistan**


**2023**

## THESIS ACCEPTANCE CERTIFICATE

Certified that final copy of MS thesis written by **Mah Roosh** (Registration No. **00000331027**), of **School of Natural Sciences** has been vetted by undersigned, found complete in all respects as per NUST statutes/regulations, is free of plagiarism, errors, and mistakes and is accepted as partial fulfillment for award of MS/M.Phil degree. It is further certified that necessary amendments as pointed out by GEC members and external examiner of the scholar have also been incorporated in the said thesis.



Signature:  \_\_\_\_\_  
Name of Supervisor: Dr. Shahid Iqbal  
Date: 09/08/2023

Signature (HoD):  \_\_\_\_\_  
Date: 10/08/2023

Signature (Dean/Principal):  \_\_\_\_\_  
Date: 11/8/2023

**National University of Sciences & Technology****MS THESIS WORK**

We hereby recommend that the dissertation prepared under our supervision by: Mah Roosh, Regn No. 00000331027 Titled: Engineering an Interfacial 2-D S-Scheme Heterojunction for Enhanced Photocatalytic Degradation of 4-Nitrophenol be Accepted in partial fulfillment of the requirements for the award of **MS** degree.

**Examination Committee Members**1. Name: PROF. MANZAR SOHAILSignature: 2. Name: DR. MUHAMMAD ADIL MANSOORSignature: Supervisor's Name DR. SHAHID IQBALSignature: 

  
Head of Department

10/08/2023  
Date

**COUNTERSIGNED**

Date: 11/8/2023

  
Dean/Principal

*Dedicated to my family*

## *Acknowledgements*

Many thanks to Allah Almighty who has provided me the ability and strength to complete my degree ,Who is the most beneficent, most merciful.

I am grateful to my worthy supervisor Dr. Shahid Iqbal and my GEC members Dr. Muhammad Adil Mansoor and Dr. Manzar Sohail for their valuable time and constructive suggestions. I am very thankful to rest of the SNS faculty members for providing a peaceful environment to me.

I owe my profound gratitude and special thanks to my research group, Safdar Bhae, and lab fellows for providing a friendly environment inside the lab.

I really appreciate all the facilities that are provided by SNS-NUST, that enabled me to complete my thesis timely.

I pay heartfelt gratitude to my parents, and my husband for their prayers, exceptional support and immense care at every moment without which it would have not been possible for me to complete my degree.

**Mah Roosh**

## **Abstract**

The treatment of contaminated water has become the biggest challenge nowadays. Thus, the removal of organic pollutants from the waste water via the use of photocatalysts is in progress. This study entails the synthesis and characterization of two-dimensional novel S-Scheme binary and ternary heterojunction photocatalysts for the photodegradation of 4-nitrophenol from wastewater. The 2-D Bi<sub>2</sub>O<sub>3</sub>/CdS and MoS<sub>2</sub>/Bi<sub>2</sub>O<sub>3</sub>/CdS S-Scheme heterojunctions were synthesized successfully via a solvothermal approach. Their structure, morphology, valency, composition, and light absorbance were characterized by XRD, HR-TEM, SEM, EDX, XPS, UV-VIS spectroscopy. The photodegradation was performed using a 1000W Xe lamp as a light source and results obtained showed that Bi<sub>2</sub>O<sub>3</sub>/CdS showed 86% degradation of 4-nitrophenol while the MoS<sub>2</sub>/Bi<sub>2</sub>O<sub>3</sub>/CdS showed excellent activity with degradation of 99% was achieved in 120 mins. These results are far better than the pure catalyst activity and the heterojunction showed exceptional results that are not known in the literature.

## List of Abbreviations

DRS	Diffuse reflectance spectroscopy
EDX	Energy dispersive X-ray spectroscopy
eV	Electron volt
TEM	Transmission electron Microscopy
SEM	Scanning electron microscopy
CdS	Cadmium Sulfide
MoS <sub>2</sub>	Molybdenum Sulfide
UV-Vis	Ultraviolet visible spectroscopy
XRD	X-Ray diffraction
XPS	X-Ray Photoelectron Spectroscopy

# Contents

## Chapter#1

### 1. Introduction

1.1 Environmental pollution .....	1
1.2 Water Pollution .....	2
1.2.1 Sources of water Pollution .....	2
1.3 Dyes .....	3
1.3.1 Classification of Dyes .....	3
1.3.2 Hazards of dyes .....	4
1.4 Heavy Metals .....	4
1.4.1 Organic Pollutants .....	5
1.4.2 Inorganic Pollutants .....	5
1.5 4-Nitrophenol .....	6
1.6 Photocatalysis .....	7
1.6.1 Working Principle .....	7
1.6.2 Types of Photocatalysis .....	8
1.6.3 Band Gap .....	8
1.7 Photocatalyst .....	9
1.7.1 Bi <sub>2</sub> O <sub>3</sub> .....	9
1.7.2 CdS .....	10
1.7.3 MoS <sub>2</sub> .....	11
1.8 S-Scheme Heterojunction .....	12
1.8.1 Charge Transfer Mechanism .....	13
1.8.2 Degradation Mechanism .....	14
1.8.3 Synthesis Methods of Photocatalysts .....	15
1.9 Characterization of the catalysts .....	16
1.9.1 Scanning electron microscope .....	16
1.9.2 EDX .....	17



1.9.3 X- ray diffraction (XRD) .....	18
1.9.4 UV-visible absorption spectroscopy .....	21
1.9.5 X-Ray photoelectron spectroscopy.....	21
1.9.6 Objectives of thesis .....	23

**Chapter 2 Literature Survey**

2.1 Synthesis of CdS Nanosheets and it’s applications .....	24
2.2 Synthesis of Bi2O3 and it’s applications .....	25
2.3 Synthesis of MoS2 and it’s applications .....	27

**Chapter 3 Experimental work**

3.1 Synthesis of Bi2O3 nanoflakes .....	28
3.2 Synthesis of CdS nanosheets.....	29
3.3 Synthesis of MoS2 .....	30
3.4 Synthesis of Bi2O3/CdS nanocomposite .....	31
3.5 Synthesis of MoS2/Bi2O3/CdS nanocomposite .....	32

**Chapter 4: Results and discussion**

4.1 X-ray Diffraction (XRD) .....	34
4.2 XPS .....	37
4.3 BET .....	40
4.4 SEM .....	41
4.5 EDX .....	42
4.6 Uv-vis DRS.....	46
4.7 Degradation Studies .....	50
4.8 % Efficiency of photocatalysts .....	52

**Chapter 5: Conclusions and future recommendations 53**

References

# List of Figures

Figure 1. Point and Non-point sources of pollution. ....	2
Figure 2 Flow chart representing classification of dyes... ..	3
Figure 3. Molecular structure of 4-nitrophenol. ....	5
Figure 4. Different morphologies of CdS .....10	10
Figure 5. Charge transfer mechanism in S-Scheme heterojunction. ....	7
Figure 6. Degradation mechanism of photocatalyst.....	10
Figure 7. Working principle of SEM.....	13
Figure 8. Illustration of how EDX works ..... 14	14
Figure 9. Schematic representation of X-Ray Diffraction Analysis .....	15
Figure 10. Scattering of incident light in XRD.....	27
Figure 11. Schematic illustration of uv-vis /DRS spectrophotometer .....	32
Figure 12. Synthetic Scheme of Bi <sub>2</sub> O <sub>3</sub> .....	36
Figure 13. Flow Chart of CdS synthesis.....	37
Figure 14. Synthetic Scheme of Bi <sub>2</sub> O <sub>3</sub> /CdS .....	37
Figure 15. Synthetic Scheme of MoS <sub>2</sub> /Bi <sub>2</sub> O <sub>3</sub> /CdS .....	38
Figure 16. Diffraction pattern of (a) CdS (b) Bi <sub>2</sub> O <sub>3</sub> (c) Bi <sub>2</sub> O <sub>3</sub> /CdS in XRD .....	38
Figure 17. XRD pattern of (d) MoS <sub>2</sub> , (e) MoS <sub>2</sub> /Bi <sub>2</sub> O <sub>3</sub> /CdS .....	39
Figure 18. XPS spectrum of Bi <sub>2</sub> O <sub>3</sub> /CdS .....	37
Figure 19. XPS spectrum of MoS <sub>2</sub> /CdS/Bi <sub>2</sub> O <sub>3</sub> .....	38
<u>Figure 20.</u> BET of MoS <sub>2</sub> , CdS, Bi <sub>2</sub> O <sub>3</sub> , Bi <sub>2</sub> O <sub>3</sub> /CdS, MoS <sub>2</sub> /Bi <sub>2</sub> O <sub>3</sub> /CdS .....	39
Figure 21. SEM images of different photocatalysts.....	41
Figure 22. EDX spectrum of CdS .....	42
Figure 23. EDX spectrum of Bi <sub>2</sub> O <sub>3</sub> .....	43
Figure 24. EDX spectrum of MoS <sub>2</sub> .....	43
Figure 25. EDX spectrum of Bi <sub>2</sub> O <sub>3</sub> /CdS.....	44
Figure 26. EDX spectrum of CdS/Bi <sub>2</sub> O <sub>3</sub> /MoS <sub>2</sub> . ....	44
Figure 27. TEM and Elemental Mapping of CdS/Bi <sub>2</sub> O <sub>3</sub> . ....	45
Figure 28. TEM and Elemental Mapping of MoS <sub>2</sub> /Bi <sub>2</sub> O <sub>3</sub> /CdS .....	46
Figure 29. DRS analysis of the synthesized photocatalysts. ....	46
Figure 30. Thermogram of MoS <sub>2</sub> ,CdS,Bi <sub>2</sub> O <sub>3</sub> , Bi <sub>2</sub> O <sub>3</sub> /CdS, MoS <sub>2</sub> /Bi <sub>2</sub> O <sub>3</sub> /CdS .....	48
Figure 31. Bar Chart showing the Efficiency of photocatalyst in 4 cycles.....	48
Figure 32. Uv-vis spectrum of Different photocatalysts( 30mg each in 100ppm pollutant solution).....	50
Figure 33. Graphs Showing % Degradation Efficiency of photocatalysts for 4-nitrophenol. 51	51

## **Chapter 1:**

### **Introduction**

#### **1.1 Environmental pollution**

Out of millions of species existing on earth, humans are the dominating ones over all others. Human beings are the root cause of all the problems regarding either environmental pollution or climatic change. A bundle of chemicals is intentionally liberated into the environment regardless of considering their hazardous effects not only for humans but also for other creatures existing on the planet Earth. Sustainable methods for the efficient degradation of these environmental pollutants are the need of the day. In this work, we have focused on the photocatalytic degradation of 4-nitrophenol.

Pollution can be defined as the existence of undesirable substances in a certain quantity or chemical composition in the environment that affects the normal functioning of processes in nature and causes various health and environmental hazards. Chemical compounds and their side products from various sources are polluting the soil, air, and water. Wastes from agricultural and industrial sources are polluting the water making it unsuitable for plants, humans, and animals. Human activities like mining, deforestation, littering, and construction are the serious cause of land pollution and are involved in the deterioration of the Earth's surface. The hazardous smoke from fossil fuel burning, traffic, and industries are involved in polluting the air directly.

The term environmental pollution is directly attributed to three components; air, soil, and water. The effects on the ecosystem may be acute, i.e. short-term or chronic. i.e. long-term. Thus, anything that affects the lithosphere, hydrosphere, and atmosphere is regarded as environmental pollution. Pollutants can be chemical compounds or toxic gases that cause undesirable physical phenomena such as green house gases causing global warming [1].

## 1.2 Water Pollution

The survival of living things is not possible without water. Marine water is not acceptable for drinking because of the high salt content in it. Aquatic and underground water is drinkable in quality.  $\frac{2}{3}$ <sup>rd</sup> of our body is comprised of water and brains are comprised of 95% water [2] and even 2% of the body's water loss leads to dehydration which inturn disturbs the anatomy and physiological functions [3]. The hazardous substances present in water make it unfit for drinking by humans and aquatic life [4]. Studies have shown the existence of large quantity of Nitrogen and Phosphorus that has come from rivers and streams [5]. Pakistan is ranked 80/122 countries for facing water difficulties especially drinking water [6].

### 1.2.1 Sources of Water pollution

A report in 1990 by the EPA shows that >50% of the contamination is caused by the leaching of toxic chemicals from landfills [6]. Mining, household sewage, industrial effluents, etc are the point sources of water pollution. Non-point sources are fertilizers, pesticides, and animal wastes[7].

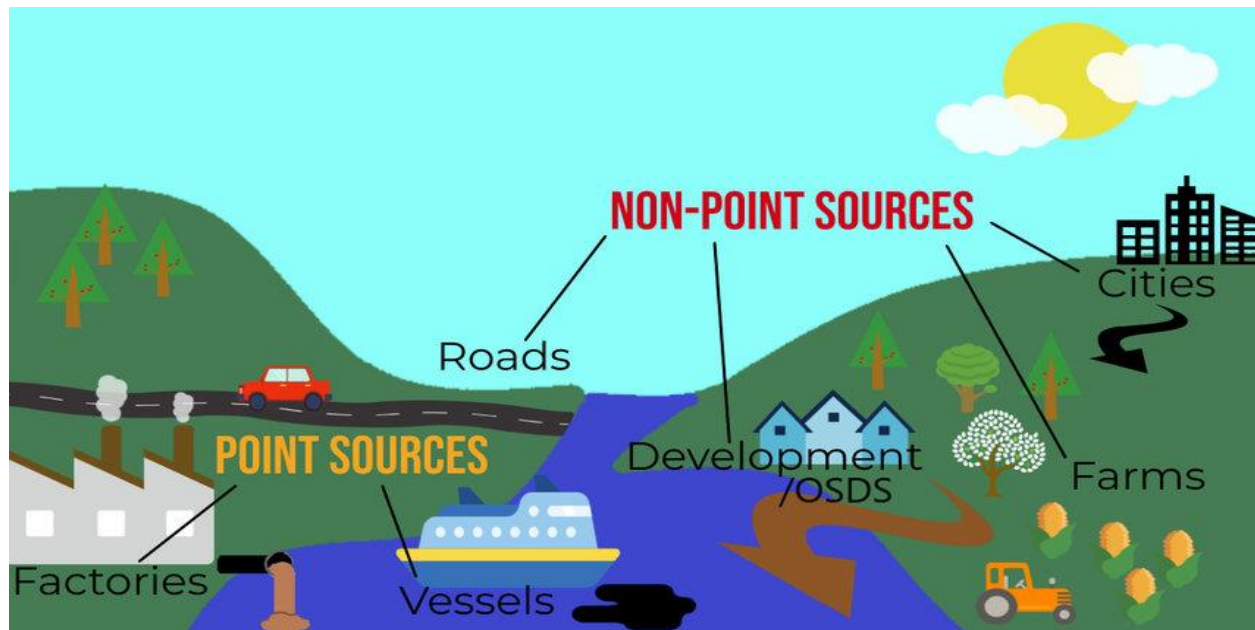


**Fig.1:** Point and non-point sources of pollution [8]

## 1.3 Dyes

Dyes are water-soluble organic compounds that are organic and ionizing in nature. They can be distinguished based on origin into two types, i.e. synthetic and natural. Natural dyes are derived from nature, i.e. plant or animal origin while synthetic dyes are further comprised of two types, i.e. azo and non-azo dyes [9]. The dyes are primarily pigments that are used for coloring substances and mostly used to color fibers and leather-made products. Dyes are the aromatic compounds that possess an affinity for the particulate substances and the most commonly used form of dyes is the aqueous form[10]. They are water-soluble because of the presence of auxochromes, i.e. -OH, -Br, -Cl, -COOH, -NO<sub>2</sub>, -NH<sub>2</sub>, -NHR, etc. in the structure. Dyes can be soluble in water only when they produce ions in water means ionization is necessary for solubility and this solubility can be achieved by the presence of auxochromes in them which are responsible for the intensification of the color of dyes. Auxochromes may be acidic or basic based on nature and their charge [11].

### 1.3.1 Classification of Dyes:

Dyes can be natural or synthetic, the former having plants and animals as sources e.g. Madder and Tyrian purple extracted from madder root and sea snails respectively whereas the latter is derived from man-made sources[12].

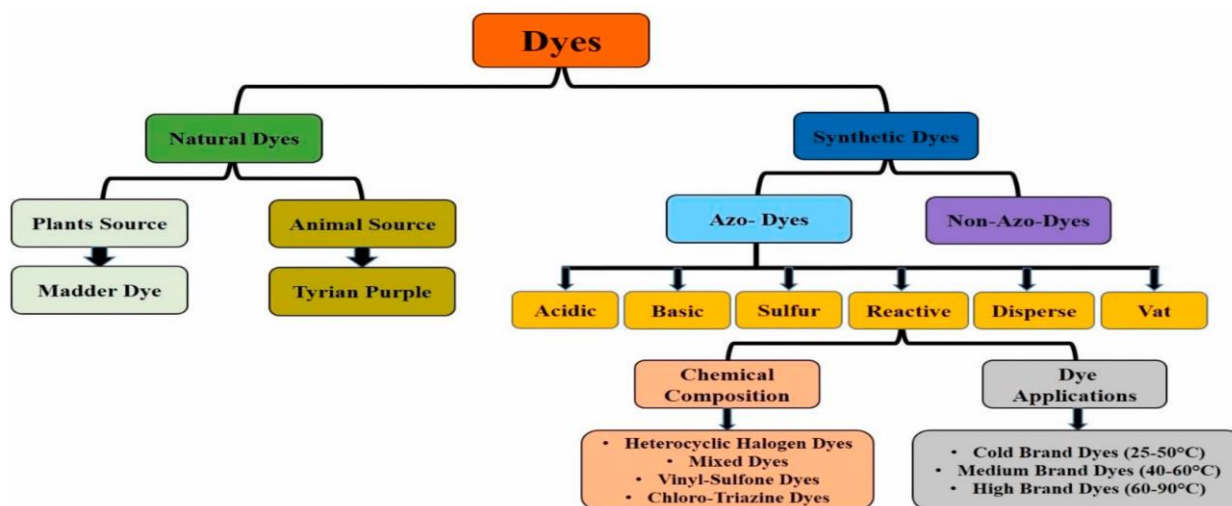


**Figure 2.** Flow chart representing the classification of dyes[13].

### **1.3.2 Hazards of dyes**

Some of the hazards of dyes are as follows [14]:

1. Most of the dyes are soluble in water and when released by industries into the water bodies are responsible for water pollution.
2. Dyes also affect the under water photosynthesis by influencing the sunlight's reflection and absorption from water.
3. Dyes pollute the water bodies even when present in a minute concentration that is not visible by the naked eye and affect the transparency of water bodies.
4. The most common hazard of reactive dyes is respiratory problems due to the inhalation of dye particles. Sometimes they can affect a person's immune system. This is called respiratory sensitization and symptoms include itching, sneezing, watery eyes, and symptoms of asthma such as wheezing and coughing.[15]
5. Many dyes possess cancer-causing abilities hence, are carcinogenic.
6. Some of the dyes are skin-irritant.

### **1.4 Heavy Metals**

The specific gravity of heavy metals is 5 times greater than water similar to Arsenic, Lead, Mercury, and Cadmium [16] which are included in the list of EPA's most dangerous substances. The majority of the metals present in the environment are heavy metals [17]. Heavy metals such as Cr, Pb, Cd, As, Cu are frequently present in industrial wastes [18,19], these poisonous metals present in wastewater menace human life and the environment. Their removal from the wastewater requires utmost attention because they are responsible for CNS disorders, stunted growth, organ damage, mortality, and malignancy [20]. The most dangerous thing about HM is that they initiate autoimmunity in which the immune system attacks itself which leads to rheumatoid arthritis, damaged nervous system, kidney damage, brain damage, etc [21]. Waste water has less concentration of HM in it, i.e.1-100mg/L at neutral or acidic pH

values, and their density in waste water surpasses 5g/cm<sup>3</sup> [22]. Electrical manufacturers are made up of Copper that pollutes the water and makes it toxic causing diarrhoea, vomiting, cramps etc [23].

#### **1.4.1 Organic Pollutants**

Few common organic pollutants are;

- Detergents
- Pharmaceutical drugs
- Pathogenic Bacteria
- Herbicides and insecticides
- Waste after food processing
- Petroleum
- Organic-compoundse.g.solvents
- Textile dyes

#### **1.4.2 Inorganic Pollutants**

HM when present more than their optimal concentration can cause extreme health effects for humans and aquatic life. The garbage from factories and homes contaminates the water and leads to various health conditions such as Airway infections, earaches, skin irritations, stomachaches, hepatitis, vomiting, encephalitis, gastroenteritis, pink eye, and diarrhea. Some of the common Inorganic pollutants include;

- Heavy metals e.g. Zn, Cl, Pb, Fe, Cu
- Fertilizers( phosphates and nitrates)

- Sulfates(SO<sub>4</sub>)
- Plastic-particles
- By-productsofindustries
- Ammonia
- Domestic effluents [24,25]

### **1.5 4-Nitrophenol**

Phenol and compounds derived from it comprise a significant class of pollutants found in water due to certain properties such as stability and water solubility. Nowadays, a lot of conventional methods are existing for the degradation of phenols but each one is having a few shortcomings [26]. Phenols comprised of nitrogen have gained importance not only due to their severe hazardous effects but also due to their poisonous effects on catalysts [27]. However, the reaction kinetics and intermediates formed during the photodegradation process of nitrogen-containing phenols need to be further studied and no proper information is reported yet [28,29]. Among the vast nitrogen-containing phenols, 4-nitrophenol (4-NP) was selected as a representative of the pollutant group due to its environmental significance. 4-Nitrophenol is toxic just like the other derivatives of phenol and lies in the list of 114 organic compounds issued by EPA. It is allowed at a maximum concentration of 20 ppb in water and causes poisoning even in a very low concentration. It is a precursor for pesticide production and synthetic dyes and is also used as a herbicide or insecticide. Due to its significant water solubility i.e.,1.6 g/100 ml, it is found in wastewater discharges as well as in wells of ground water and surface waters from where it gets removed to make water drinkable [30].



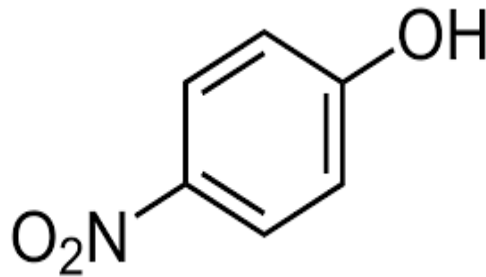


**Figure 3.** Molecular structure of 4-nitrophenol.

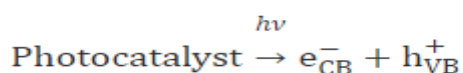
## 1.6 Photocatalysis

Photocatalyst is a term comprised of two words; photo for photon and catalyst for a rate-altering substance and the phenomenon is referred as photocatalysis. Photocatalysis deals with chemical reactions that require a photocatalyst or a semi-conductor and sunlight for the reaction to happen. A photocatalyst is a semiconductor material that is involved in the enhancement of the rate of reaction. The process of photocatalysis can be applied in a wide variety of fields such as deodorizing, antifogging, air purifying, anti-bacterial, water purification, self-cleaning, etc. It is becoming a need of the day due to its green way of providing potential solutions for the production of renewable energy as well as its cleanliness, efficiency, inexhaustibility, and cost-effectiveness. Water is a fundamental requirement of human beings, plants, and animals. Along with the population increase, urbanization, and industrialization day by day, the water demand is increasing which needs purification. For this purpose, photocatalysis is used in the treatment of wastewater and the remediation of water[31]. At present, many challenges are faced by the globe regarding life quality and the environment. One of the major challenges is water pollution which is of utmost concern and responsible for water stress and scarcity in most of countries in the world[32].

### 1.6.1 Working Principle

Photocatalysis is based on 3 important phenomena.

**1. Light Harvesting-** Absorption of photons of light to produce electron-hole pair.



2. **Charge Transfer-** Photogenerated charge carriers are excited to prevent recombination.

3. **Charge Consumption-** Chemical reactions (oxidation/reduction) are initiated [33].

### 1.6.2 Types of Photocatalysis

Based on the physical state of reactants, there are two types of photocatalytic reactions.

- **Homogeneous photocatalysis:** When the reactant(s,l,g) and the catalyst(s,l,g) are exhibiting the same phase, the reaction is termed as homogeneous photocatalysis.
- **Heterogeneous photocatalysis:** When both the reactant and catalyst are in different phases, the reaction is termed as heterogeneous photocatalysis.

### 1.6.3 Band gap(Eg)

The difference in energy that exists between the HOMO of the valence band and the LUMO of the conduction band is called the Band gap. Depending upon the band gap, materials are categorized into three categories.

- metal or conductor: Eg, 1.0 eV
- semiconductor: Eg, 1.5-3.0 eV
- insulator: Eg, 5.0 eV

Semiconductors are the substances that conduct electricity at room temperature in light's presence and act as photocatalysts. When light of a certain wavelength is irradiated on a photocatalyst, the electron of the valence band gets the energy of the photon and gets excited to the conduction band. The electron which gets excited leaves behind a hole(h1) in the valence band. Thus, a photoexcitation state is created and electron-hole pair is formed. The electron which has been excited reduces the acceptor that contains a hole for oxidizing the donor molecule. A photocatalyst simultaneously provides the oxidative and reductive environments. The substrate and the semi-conductor can interact with each other in four

different ways based on relative positions of VB, CB, and redox levels. The four different combinations are

1. Substrate undergoes reduction upon lowering of its redox level compared to CB of semiconductor.
2. Substrate undergoes oxidation upon elevation of its redox level compared to VB of the semi-conductor.
3. Substrate does not undergo oxidation or reduction in both cases, i.e. when the **substrate's redox level >CB** and when the **substrate's redox level < VB**
4. Substrate undergoes both the oxidation and reduction process when,

Conduction band > substrate's redox level > Valence Band

Due to the electronic structure, semiconductors can behave as the sensitizers for photo-redox reaction. The complete mineralization of most of the organic pollutants like dyes, halo hydrocarbons, aromatics, pesticides, insecticides, and surfactants. Semiconductor-mediated photocatalysis has acquired immense attention in terms of overcoming the problems that are related to rapid charge recombination. Organic pollutants such as 4-nitrophenol can be completely or partially mineralized by photocatalysis of semi-conductors[34].

## **1.7 Photocatalyst**

### **1.7.1 CdS**

Since metal sulfides are known to have a narrow band gap and a very suitable position of the conduction band, due to which it acts as a photocatalytic material responsive in visible light[35]. One of the most common photocatalysts is cadmium sulfide, a visible-light-responsive material having a band gap of 2.4 eV known for photodegradation of organic pollutants in water as well for photocatalytic Hydrogen production, environmental purification, fuel generation via solar light [36,37].

In the past few years, CdS has attracted much attention specifically in the field of H<sub>2</sub>

production via photocatalysis. At wavelength  $< 516\text{nm}$ , CdS exhibits superior visible light absorption while on the other hand, it possesses a good capacity for transportation of charge carriers, thus making the photogenerated holes and electrons mobile in an efficient manner, which extends the life of photogenerated charge carriers and results in higher photocatalytic activity [38]. CdS has gained immense attention because for reducing the protons it possesses the conduction band edge with sufficient negative potential. Cadmium sulfide, is among the prominent semiconductor-based photocatalysts used for solar-fuel generation, owing to its excellent optical and electrical properties. The photocatalytic properties of CdS photocatalysts have been reported with specific nanostructures, i.e. 0-dimensional, 1-D, 2-D, and 3-structures[39].

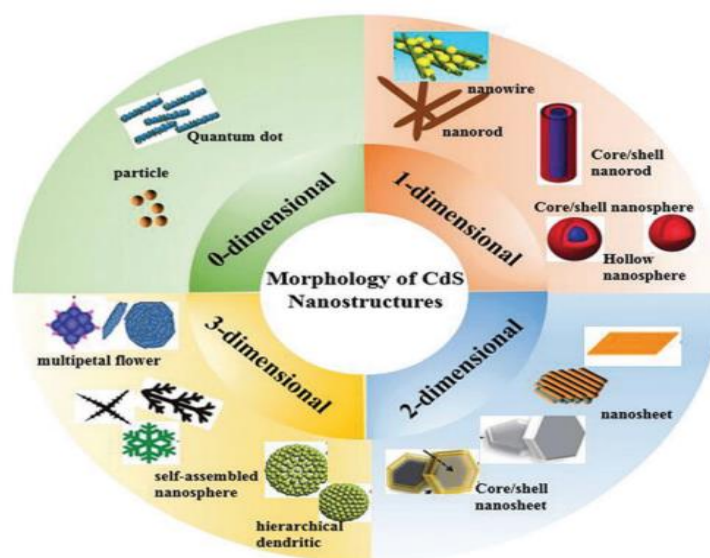


**Fig.4:** Different Morphologies of CdS

It acts as a sensitizer for wide band gap semiconductors, like  $\text{Bi}_2\text{O}_3$ , that are visible light-driven catalysts. CdS absorbs photons whose energies fall in the major portion of the solar spectrum. Several heterojunctions with CdS have been known but the efficiency is still unsatisfactory [40-42]. However, the applications of pure CdS NRs have some drawbacks, such as photo corrosion and photogenerated carriers recombining rapidly, which could be overcome by constructing an S-scheme heterojunction system [43].

### 1.7.2 Bi<sub>2</sub>O<sub>3</sub> as a photocatalyst

Bismuth-based photocatalysts can be widely used for the degradation of organic compounds via the process of photocatalysis [44,45]. Bismuth oxide (Bi<sub>2</sub>O<sub>3</sub>) exists in six polymorphic structures such as;  $\alpha$ ,  $\beta$ ,  $\delta$ ,  $\gamma$ ,  $\epsilon$ , and  $\omega$ , whereas the  $\alpha, \beta$  phases were commonly known for their photocatalytic applications. Bi<sub>2</sub>O<sub>3</sub> possesses better visible or solar light efficiency because it has a wide range absorption spectrum that lies in the visible region with a bandgap of optimum optical energy in comparison to the other metal oxides. For instance, Bi<sub>2</sub>O<sub>3</sub> has two times higher photocatalytic activity under visible light as compared to TiO<sub>2</sub> [46]. Bismuth oxide (Bi<sub>2</sub>O<sub>3</sub>) has a variety of applications such as in fuel cells of solid oxide, ceramic glass manufacturing in gas sensors, optical coatings etc., owing to their excellent properties, such as high dielectric permittivity, high refractive index, and remarkable photoluminescence properties. Bi<sub>2</sub>O<sub>3</sub> has also been known as a good photocatalyst for water-splitting applications and pollutant decomposition under visible light irradiation [47].

### 1.7.3 MoS<sub>2</sub> as a co-catalyst

Molybdenum disulfide (MoS<sub>2</sub>) nanosheets, have gained attention significantly due to their unique mechanical [48], electrical [49,50], biological [51], and physicochemical properties. With known applications in the field of electronics, biomedical [52], catalysis [53], and energy-related fields [54,55]. MoS<sub>2</sub> nanosheets possess novel applications specifically in environmental fields. Whereas, bulk MoS<sub>2</sub> is naturally found in the form of mineral molybdenite, has been used as adsorbent and environmental catalysts [56,57] since longer times.

Among the gas-sensing materials, MoS<sub>2</sub>, being a cheaper n-type semiconductor having more potential value in gas-sensor applications owing to its unique electrical, optical, and mechanical properties [58-59]. MoS<sub>2</sub> comprises of a layered structure having three layers of S–Mo–S that are bounded by the weaker Vander Waals forces, thus, producing materials with

unique properties [60]. Also, MoS<sub>2</sub> possesses a tunable band gap depending upon the number of layers of MoS<sub>2</sub>. The bulk MoS<sub>2</sub> possesses a bandgap of 1.2 eV and it increases for 2-D single-layer nanosheets and becomes 1.8eV [61,62]. This characteristic property of MoS<sub>2</sub> is crucial in improving its sensing performances [63].

## **1.8 S-Scheme Heterojunction**

### **Hetero-junction**

Heterojunction Photocatalysts are formed by the coupling reaction of two or more semiconductor photocatalysts. Thermodynamically, the major driving force for a reaction depends on the difference between V.B potential and C.B potential and that of reaction. If a single photocatalyst tends to possess a strong redox ability then it must have deep VB and high CB positions. And If it tends to possess high efficiency of light harvesting then it must possess shallow VB and low CB positions. These deficiencies of the mono-catalyst lead to the idea of the development of heterojunction [64].

Photocatalytic reactions are thermodynamically favored by S-Scheme heterojunction as it provides a major driving force due to its strong redox abilities. Photocatalysts may be oxidation photocatalysts or reduction photocatalysts depending upon band structure, the former is used in environmental degradation processes where photogenerated electrons are ineffective and holes are the contributive factors, the latter has a high conduction band with major usage in the production of solar cells producing photogenerated electrons and holes which are effective and useless (removed by sacrificial agents) respectively. A heterojunction that is based on Step-Scheme contains an OP and RP having staggered band structures[65-68].

#### **1.8.1 Charge Transfer Mechanism**

The charge transfer pathway of an S-Scheme heterojunction is as follows. Compared to OP, RP possesses higher VB and CB positions with less work function. When OP and RP

come in close proximity, the electrons from RP diffuse to OP spontaneously thus electron accumulation and electron-depletion layer is generated near the interface in OP and RP respectively. An internal electric field is created that is directed from RP(positively charged) to OP(negatively charged) is generated, which accelerates the transfer of electrons. After contact, the Fermi level of both get aligned at the same level by doing upward and downward shifts of OP and RP respectively. Due to band bending, the recombination of photogenerated es in OP's conduction band and holes in RP's Valence Band occurs due to the Coulombic force of attraction between  $h^+$  and  $e^-$ s. In short, these are the three major factors that provide the major driving force for e-hole recombination, and the unwanted holes and electrons are eliminated via recombination but the energetic holes and electrons participate in the photocatalytic reactions [69-72].

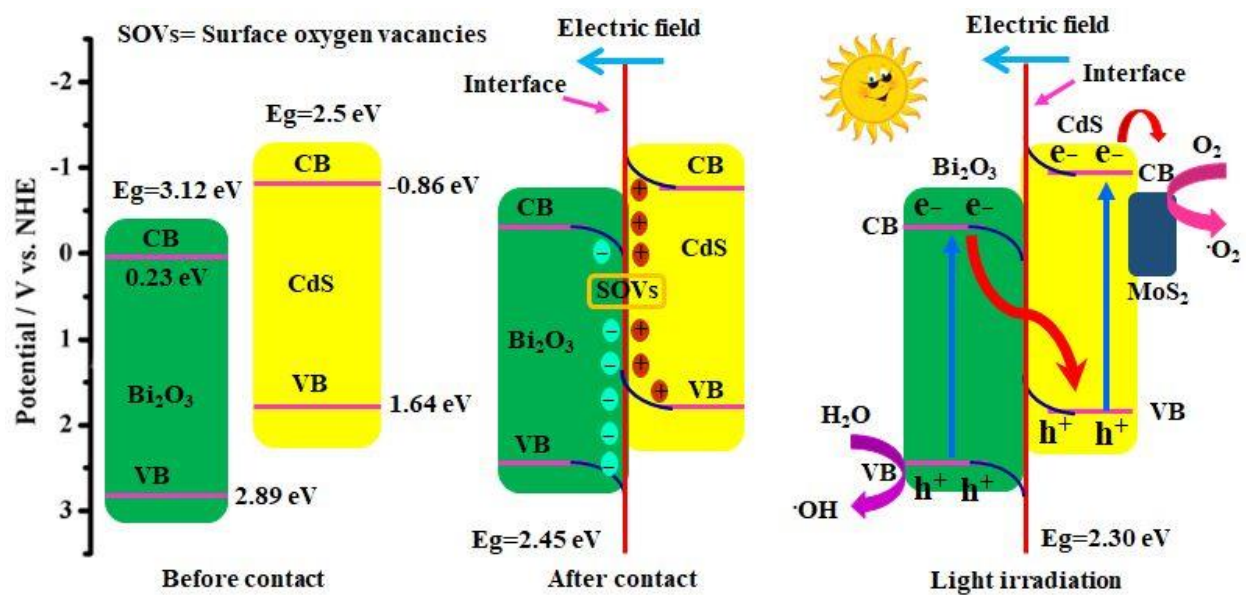


Fig.5: shows Charge transfer mechanism in S-Scheme heterojunction. (a) Before contact (b) After contact (c) Upon Light irradiation.

### 1.8.2 Degradation Mechanism

The irradiation of the semiconductor photocatalyst with light photon excites the valence band electrons, leaving a hole behind, to the CB of the photocatalyst. The excited electron reaches CB where it undergoes reduction while the hole in the VB undergoes an oxidation

process [73]. Figure(6) shows the photocatalytic mechanism of degradation.

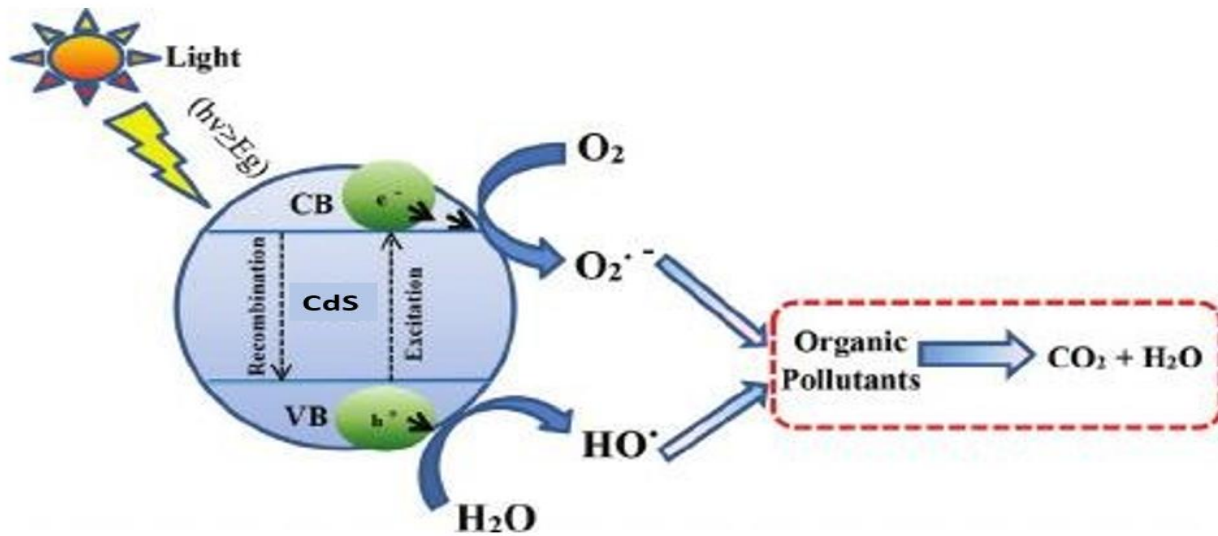


Fig.6: Degradation mechanism of a photocatalyst

### 1.8.3 Synthesis Methods of Photocatalysts

Their morphologies depend upon the method of synthesis used. Following are some of the methods used for the synthesis of photocatalysts, CdS, Bi<sub>2</sub>O<sub>3</sub>, and MoS<sub>2</sub> [74]:

1. Hydrothermal method
2. Electrodeposition
3. Solvothermal method
4. Chemical vapor deposition
5. Direct oxidation method
6. Sol-gel method
7. Chemical vapor deposition
8. Microwave method
9. Sonochemical method



## **1.9 Characterization of the catalysts**

### **1.9.1 SEM:**

Scanning electron microscope is one of the principle characterization techniques that provides info about morphology, elemental composition, and topography. In 1930, SEM was designed by Manfred von Ardenne. In SEM analysis, surface images are produced by direct scanning over a sample's surface with a high energy electron-beam. SEM is equipped with EDS that determines the elemental composition in a sample. EDS takes the data from SEM that is used to identify sample's elemental composition. The electron beam inelastically collides with the specimen and produces SE as well as X-rays. The spectrum is generated after x-rays detection showing different peaks corresponding to the different elements. In SEM, the direction of incident beam can be qualified by magnetic or electrostatic fields as a result of the convergence of primary electrons into the electron probe, which is of small diameter, used to scan the object. The probe covers a small area of the specimen such as square or rectangular area and secondary electrons released from each region of specimen as a result of concurrent scanning in two perpendicular directions, gather to produce an image of that area. This type of scanning is termed as raster scanning. The signals produced by this type of scanning are used for the deflection of a beam within Cathode Ray Tube that contains electron-gun for producing narrow beam electrons which in turn was focused onto a phosphor screen for transforming the electrons into the visible light. For controlling the intensity of beam, amplification of secondary electrons signal occurs which were then transferred to an electron gun. The phosphor screen generates light which represents the secondary electron image of the specimen since it was completely synchronized with the electron beam's speed on the specimen. Normally, the picture resolution was found to be 1-10nm which is much better as compared to a light microscope. Due to the high depth of focus, SEM focuses on those specimen characteristics that aren't in the plane

of light directly to make them distinct and clear[75].

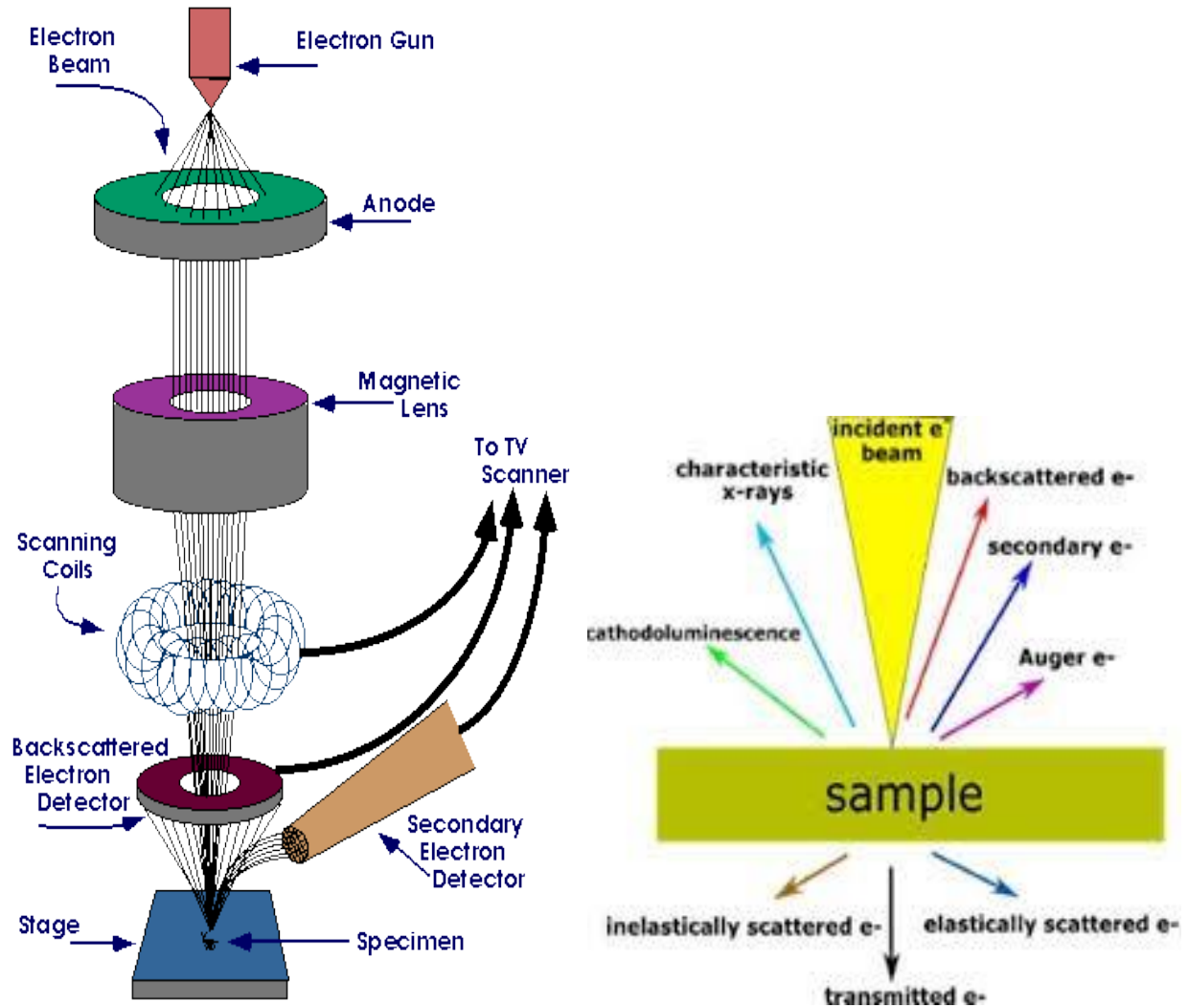
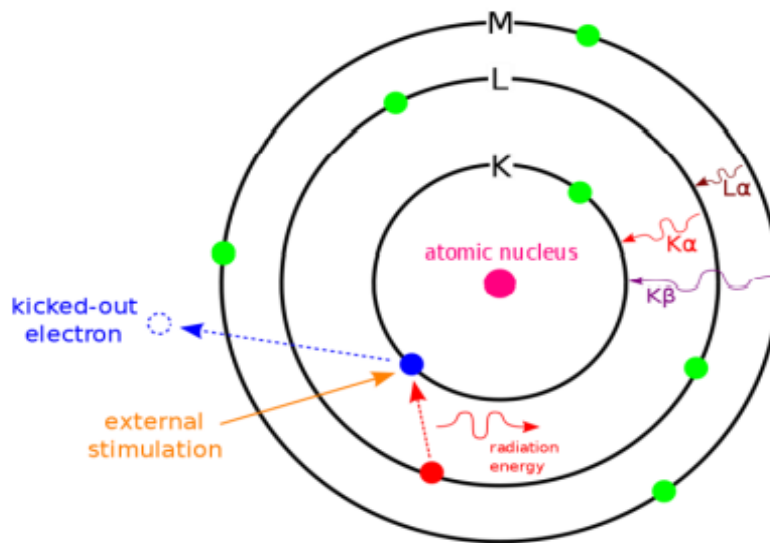


Fig.7: Working Principle of SEM

### 1.9.2 Energy dispersive spectroscopy

For determining the material's elemental composition, Energy-dispersive X-ray spectroscopy (also referred to as EDX, EDXA, or EDS) is a powerful method. EDS is based on Moseley's law that directly relates the frequency of emitted light and atom's atomic no. The operational principle of EDX is the highly accelerated x-rays are used to eject electrons from an atom, leaving behind a hole which is occupied by an electron coming from higher energy(de-

excitation) so energy is released which is a specific for each element in a periodic table. So in this way, elements in a material as well as their proportion can be determined.



**Fig 8-**An illustration of how EDS works.

The letters K, L, and M denote the principal quantum number  $n$  value of electrons in that shell (K electrons, closest to the nucleus, having  $n=1$  electrons), and  $\alpha$ ,  $\beta$  represents the transition size. The relaxation of electron from M to L-shell directly or from L to K-shell assigned as  $L\alpha$  or  $K\alpha$ , respectively, whereas the electronic transition from M to K-shell directly is assigned as  $K\beta$  transition. EDS instrument constitutes three main components: a collector, an emitter, and an analyzer, which in combination helps to study the number of radiated X-rays and their energy comparative to the initially emitted X-rays. The EDS data is represented in the form of graph, with peak intensity on y-axis, and KeV on the x-axis, linked with a computer software that is involved in conversion of peak location that is on the x-axis into the atoms that represent the energy changes [76].

### 1.9.3 X-ray diffraction

X-ray diffraction analysis is an analysis that determines the material's crystallography. Here, the material is irradiated with incoming x-rays and rays that are emitted

from the substance are measured for their scattering angles and intensities. Upon interpretation of diffraction pattern, materials can be identified. XRD graph helps us to identify phase and also gives information about the difference between the real and ideal structure due to the existing crystal defects and strains. X-rays are basically wave packets of electromagnetic energy and the ordered arrangement of atoms is referred to as crystal. The stationary source emits X-rays whereas the specimen is kept dynamic w.r.t to X-ray stream in reflection mode. The diffracted beam of electrons is collected by a detector which rapidly rotates twice along with the sample.

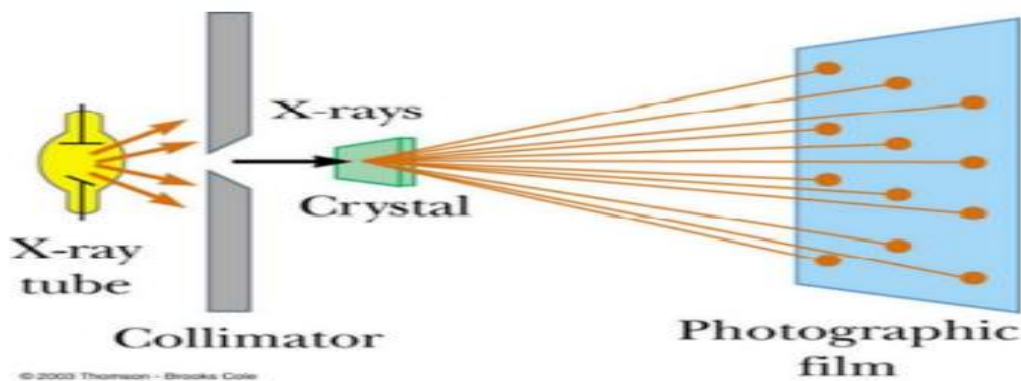


**Fig 9-** Schematic representation of X-Ray Diffraction Analysis.

The basic principle of X-ray diffraction is the constructive interference between a crystalline sample and x-rays(monochromatic). X-rays are produced by CRT and filtered to form monochromatic radiation, then the beam is focused onto the sample. Upon striking of monochromatic x-rays with the crystal, electrons inside the crystal begin to vibrate and propelled with the frequency same as that of incident x-ray. These highly energetic electrons radiate in all possible directions with the frequency same as the incident x-rays. The radiations may interfere constructively or destructively and produce orientation specific- diffraction pattern(i.e., maxima and minima). Scattering of X-rays occurs due to the interaction between crystal atoms' electrons and incident x-rays which is called elastic scattering whereas electron acts as scatterer creating an ordered array of spherical waves. The scatterers in a regular array create a regular array of

spherical waves. Due to destructive interference, these spherical waves are wiped out by each other in most of the directions due to destructive interference, whereas they do constructive interference in selected directions, in accordance with Bragg's law;

$$2d\sin\theta = n\lambda.$$

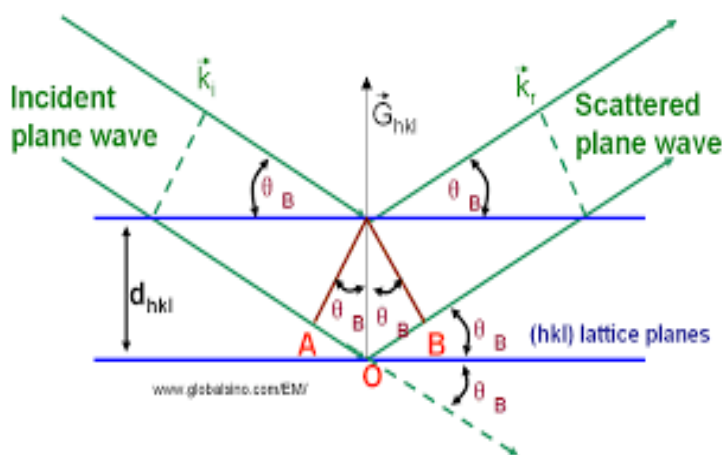


**Fig.10:** Scattering of incident light in XRD

Where;

$d$  is distance between diffracting planes,

$\theta$  (theta) denotes the incidence angle,

$n$  denotes an integer,

and  $\lambda$  is wavelength of the beam.

$d$ -spacings are determined by the directions at which the maxima are detected and the exact directions create reflections on a diffraction pattern. The diffraction patterns emerge due to the impinging of electromagnetic waves on array of scatterers. Since the wavelength ( $\lambda$ ) of X-rays is of the same order of magnitude as the interplanar crystal spacing ( $d$ ) i.e, 1-100 angstroms, X-rays are involved in creation of the diffraction pattern. Thus, making Use of database library that are included with the XRD programme, the structural parameters and crystal category of a sample can be determined by computing the  $d$ -spacings of several peaks.

The p-XRD analysis of all the samples was performed on Advanced Bruker D8, x-ray diffractometer with Cu  $K\alpha$  x-ray source ( $\lambda = 1.5405\text{\AA}$ ) in  $2\theta$  range of 5-80°. The Scherer

equation is used to calculate the average crystallite size as given below:

$$D = \frac{K\lambda}{\beta \cos\theta}$$

Where

D is the Crystallite size

$\lambda$  is the wavelength (Cu K $\alpha$  = 1.5405Å)

$\beta$  is FWHM (rad)

$\theta$  represents peak position (rad) [77]

#### 1.9.4 UV-Visible absorption spectroscopy

Uv-vis or DRS is a technique that involves light absorption by a molecule in the 200-800nm range causing electronic excitation from the ground to an excited state. Light energy is absorbed by molecules possessing  $\pi$  or n-electrons so that the electrons get excited to ABMO. More longer the wavelength absorbed by an electron, the more easily es gets excited resulting in electronic transitions such as; n- $\sigma^*$ ,  $\sigma$ - $\sigma^*$ ,  $\pi$ - $\pi^*$ , n - $\pi^*$ . A spectrum is developed due to the absorption of light that helps to identify a compound.

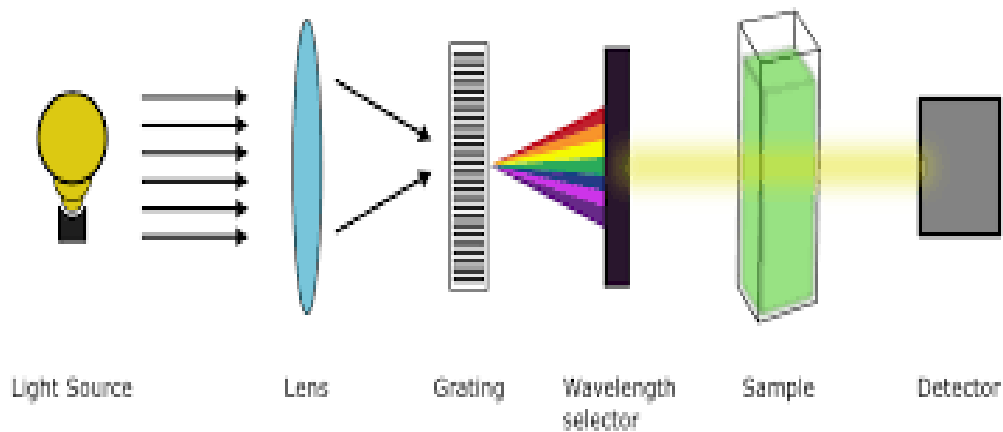


**Fig.11:** Schematic illustration of uv-vis /DRS spectrophotometer [78]

#### 1.9.5 XPS

A quantitative technique that provides the surface analysis of a material. The basic

principle of this surface-sensitive technique is when an x-ray beam irradiates a sample under vacuum, the no of electrons run-off from the material's surface and their kinetic energy are measured simultaneously. The spectrum is obtained that gives information about the empirical formula, composition, and electronic and chemical states of elements present in a material[79].

### **Objectives of thesis**

The prime objective of this research work is the photodegradation of 4-nitrophenol pollutants.

The detailed objectives are enlisted below:

1. To develop an efficacious material using hydrothermal methods for the reduction of environmental pollution.
2. Fabrication of 2-D S-Scheme CdS/Bi<sub>2</sub>O<sub>3</sub>/MoS<sub>2</sub> ternary nano-heterojunction for enhanced photocatalytic applications.
3. Visible light-driven catalyst for degradation of organic pollutants, such as 4-nitrophenol from water.

## Chapter 2

### Literature Survey

#### 2.1 Synthesis of CdS

One of the most common visible light-responsive photocatalysts is Cadmium sulfide having a band gap of 2.4eV widely used for the generation of solar fuels owing to its excellent electrical and optical properties that are known for photocatalytic H<sub>2</sub> production. CdS-based photocatalysts are extensively applicable in various fields such as in CO<sub>2</sub> reduction, pollutant degradation, and hydrogen production [80, 81,82,83].

Cadmium Sulfide being a good visible light-absorbing photocatalyst at  $\lambda < 516\text{nm}$  possesses a very efficient transportation capacity of charge carriers that provides mobility to the photogenerated holes and electrons in a timely fashion by increasing the lifespan of charge carriers resulting in increased photocatalytic activity [84].

The hexagonal 1-D CdS nanorods were prepared via a one-pot method using a solvent and the precursors used for synthesis were thiourea and Cd(NO<sub>3</sub>)<sub>2</sub>·4H<sub>2</sub>O as sulfur and Cadmium sources, respectively. The method is advantageous in the sense that it leads to the formation of the hexagonal 1-D structure of CdS deposited with Pt simultaneously. The hydrogen production rate varies considerably upon changing the amount of Pt loaded. Pt-deposited CdS was proven to have enhanced hydrogen production efficiency whereas the Pt serves as a co-catalyst [85].

CdS has been used in the field of photocatalysis for a longer time, it is because the conduction band edge position of CdS is more negative than most of the other known photocatalysts, providing a greater reduction power to photogenerated es of CdS. The catalytic efficiency of the pure CdS semi-conductor doesn't meet the requirements for practical applications due to the less adsorption capacity of CdS towards reactants, compact inter particle aggregation, poor photostability that increases the rate of recombination of charge carriers by decreasing the surface area that is not desirable for photocatalytic activity improvement [86].



The hollow structured CdS nanomaterials are among the promising photocatalysts that are featured with enhanced ability of light absorption, more active sites available for redox reactions, and a large surface area leading to a broader application prospect [87].

The hollow Cadmium Sulfide photocatalysts possess unique photocatalytic activity towards H<sub>2</sub> production, CO<sub>2</sub> reduction in visible-light, and pollutant degradation. Due to the hollow structure, some properties get enhanced, for-instance; surface area, number of available active sites, and decreased diffusion length for mass-to-charge transfer. Such structure allows intensive light absorption due to reflection and scattering in the interior cavities resulting in exceptional photocatalytic performance [88,89,90,91]. The hierarchical nanosheets that assemble to form a flower-like morphology of CdS were prepared via the ion-exchange method. The main starting materials used for synthesis were Na<sub>2</sub>S and Cd(OH)<sub>2</sub> as sources of Sulphur and Cadmium respectively for the photodegradation of Rhodamine- B dye [92].

The ultrathin CdS nanosheets have been prepared possessing a thickness of approximately 4 nm via an ultrasonic-assisted aq exfoliation method that involves the lamellar CdS–DETA hybrid nanosheets as a precursor material whereas L-cysteine is used as a stabilizer. The as-obtained ultrathin sheets of Cadmium Sulfide exhibit outstanding photocatalytic activity with reasonable stability for hydrogen production [93]. Cadmium sulfide (CdS) nano-crystalline morphologies were prepared via solvothermal method at temperatures (200, 160, 120, and 100 °C) for 7 h in ethylenediamine solvent. Two different morphologies of CdS were synthesized: nanosheets at a temperature of 100 and 120 °C and nanowires at 160°C and 200 °C. The hexagonal wurtzite nanowire diameter is tens of nanometers, while the length ranges from several micrometers. CdS nanosheets prepared at varying temperatures (100 and 120) have optical band gaps of 3.25 and 2.42eV respectively whereas the nanowires synthesized at 2.55 and 2.59eV at temperatures of 160 and 200°C respectively [94].

## **2.2 Synthesis of Bi<sub>2</sub>O<sub>3</sub>**

Single crystal bismuth oxide nanoflakes were prepared with a bismuth oxalate as a precursor. During the synthetic procedure, the precipitate of bismuth oxalate was treated hydrothermally, and the pH was varied which affects the morphology and crystal phase of the precursor. The tetragonal  $\beta$ - $\text{Bi}_2\text{O}_3$  and monoclinic  $\alpha$ - $\text{Bi}_2\text{O}_3$  were obtained depending on the calcination temperature and crystal phases of precursors. It was tested for the photocatalytic degradation of Rhodamine-B and it was found that activity varies by changing the morphology of the material [95]. A flower-like shape of  $\alpha$ - $\text{Bi}_2\text{O}_3$  doped with Na was prepared hydrothermally. The samples comprise crystallized nanoplates possessing smooth surfaces and thicknesses of the order of tens of nanometers. Due to doping with Na, the photocatalytic activity regarding the photodegradation of Rhodamine-B dye was improved significantly owing to the induced oxygen vacancies. This synthetic approach is advantageous owing to its simplicity, lack of post-sintering, low reaction time, huge scale production, template-free, cost-effectiveness, etc [96].

The solvothermal method was chosen for the efficient synthesis of  $\beta$ - $\text{Bi}_2\text{O}_3$  nanoflakes. At 350°C, the Cassandra flower morphology was obtained by the uniform distribution of heat during the calcination, allowing the growth of material along the c-axis. The material synthesized was partially agglomerated, owing to the electrostatic attractive forces. The synthesized material was effective for the degradation of bromocresol Purple and Bromothymol Blue showing the degradation efficiency of 94% (200min) and 96% (160min) [97].

### **2.3 Synthesis of MoS<sub>2</sub>**

The hollow flower-like microspheres of MoS<sub>2</sub> were synthesized by using a surfactant. The morphology is affected by the surfactant amount and reaction time. The procedure involves the use of surfactant, Na<sub>2</sub>MoO<sub>4</sub>, Na<sub>2</sub>S, and NH<sub>2</sub>OH•HCl as reagents and ultra-pure water as solvent under hydrothermal conditions [98]. Molybdenum Sulfide nanowires have been prepared hydrothermally having a diameter and length of 4nm and 50nm respectively. The synthesis

involves the use of 1.8 g  $\text{Na}_2\text{S}$  and 0.36g  $\text{MoO}_3$  at  $260^\circ\text{C}$ . It was observed that the  $\text{MoS}_2$  nanowires possess 1-10 sulfide layers but it's formation and specifically the morphology is strongly affected by exterior conditions such as; temperature, pH, and concentration [99].

It was reported that the hollow tubular  $\text{MoS}_2$  having a uniformly controlled size and shape with a length of approx 30nm, diameter 50 nm, and wall thickness 10 nm were prepared with a controllable size distribution of nanotubules or fibers via a template. The template has a specific pore size that is limited thus, nanowires of diameter < 50nm couldn't be produced [100, 101].

## Chapter 3

### Experimental Section

#### 3.1 Synthesis of Bi<sub>2</sub>O<sub>3</sub>:

Bi<sub>2</sub>O<sub>3</sub> as prepared by a solvothermal synthetic approach by using a mixture of solvents( ethanol, ethylene glycol, water). In a typical synthesis procedure, a cationic surfactant; Cetyl trimethyl ammonium bromide(CTAB) is used for controlling morphology.

1. CTAB(0.05g) was dissolved in a mixture of solvents. i.e. Ethanol-water in 18:17 upon vigorous stirring for 20mins so that the lather is produced due to surfactant
2. Then 390mg of BiNO<sub>3</sub>.5H<sub>2</sub>O is added to the above solution to form a transparent solution.
3. After that, 36ml of Ethylene Glycol was added to the transparent solution upon stirring which was continued for 20mins.
4. The resultant solution was placed for the aging at r.t for a duration of 24hrs.
5. After the completion of aging period, the mixture was stirred for 5 mins and then poured in the Teflon steel lined autoclave (100ml) fulfilling 3/4<sup>th</sup> of its volume at 170° C for 5hrs.
6. The product was separated from solvent using centrifugation which was done at 8000 rpm for 6mins then washed thrice with ultrapure pure water as well as with ethanol.
7. Finally, the white-colored product was placed for vacuum drying at 65°C in a time period of 3-4 hrs.
8. The product was then thermally treated under Argon and air flow at 400°C at a rate of 2.5 C/min (ramping time 160mins) for 30mins(reaction time) in a muffle furnace. Upon calcination, the white color of Bi<sub>2</sub>O<sub>3</sub> changed from white to yellow thus, confirming the formation of Bismuth oxide.

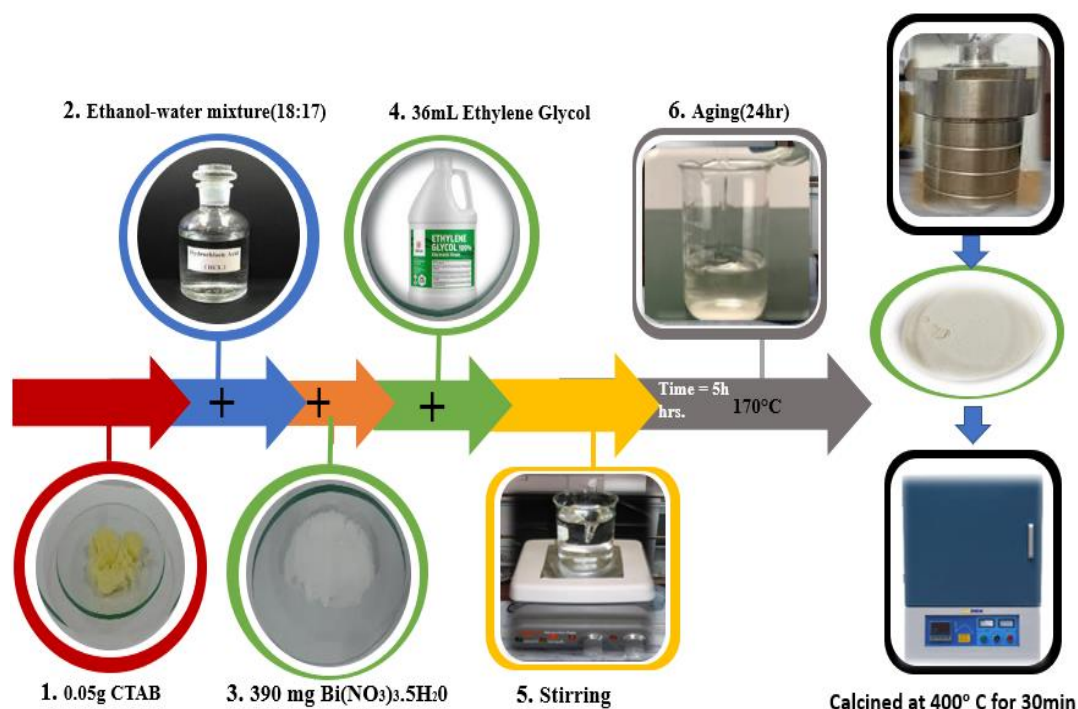


Fig.12: Synthetic Scheme of Bi<sub>2</sub>O<sub>3</sub>

### 3.2 Synthesis of CdS:

Anhydrous Cadmium Acetate, Cd(CH<sub>3</sub>COO)<sub>2</sub>, was used as a source of Cd and Thiourea, CH<sub>4</sub>N<sub>2</sub>S, as a sulfur source and solvothermal synthesis was performed using Ethylene diamine (en) as a solvent.

1. Initially, 0.533g of Cd(CH<sub>3</sub>COO)<sub>2</sub> was dissolved in 60ml of en upon stirring for an hour.
2. After that, 0.448g of Thiourea was added subsequently and the mixture solution was further stirred for 30mins.
3. The whole mixture solution was then poured in 100ml Teflon, such that 3/4<sup>th</sup> of the volume of an autoclave get occupied by solution, which was placed in a heating oven at 105 C for 8hrs.
4. The autoclave undergoes auto-cooling after the assigned time period and the product was centrifuged at 8000rpm for 8 mins subsequently followed by washing thrice with deionized water and commercial-grade ethanol to eliminate any organic and inorganic impurities.
5. The product was placed for drying at 60°C in a vacuum oven overnight and the yellow-colored

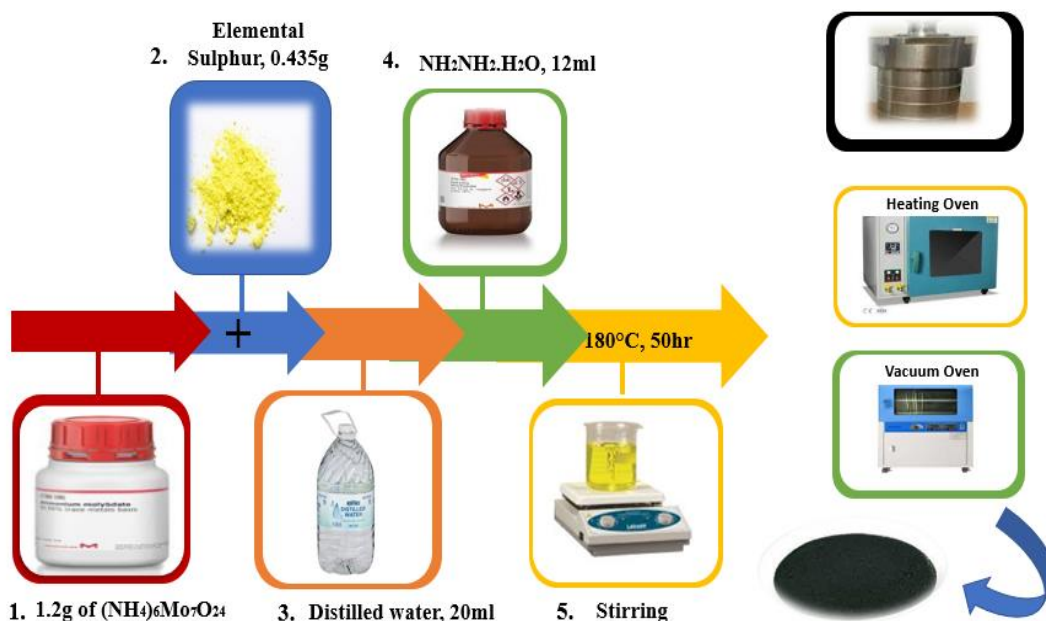
product was obtained and yield is 0.10g.



Fig.13: Flowsheet of CdS synthesis

### 3.3 Hydrothermal Synthesis of MoS<sub>2</sub>

Molybdenum sulfide was formulated by a facile hydrothermal method. For this, all the chemical used were analytical grade and of the Sigma-Aldrich. Molybdenum and Sulphur sources were needed for this purpose, i.e; Ammonium Molybdate ( $(\text{NH}_4)_6\text{Mo}_7\text{O}_{24}\cdot 4\text{H}_2\text{O}$ ) as a Molybdenum source and Elemental Sulphur as a Sulphur source. In a typical synthetic procedure, 2.4 g of Ammonium Molybdate and 0.87g of Elemental Sulphur powders were mixed and finely grounded and added into a 100ml beaker containing 40ml of ultrapure water upon stirring. Then 24ml of Hydrazine Monohydrate(85%), a reducing agent, was dropwise added into the solution and continuously stirred for 30mins. The mixture solution was then poured into 100ml autoclave such that the solution occupies  $\frac{3}{4}$ <sup>th</sup> of the total volume of an autoclave. Then the autoclave is tightly sealed to build-up autogenous pressure and placed in a heating oven at 180 degree Celsius for 50hr. The autoclave was cooled at room temperature and the product was obtained which was then centrifuged at 8000 rpm for 6 mins and subsequently followed by washing with deionized water thrice and twice with commercial ethanol. The final black colored product was obtained which was dried in a vacuum oven at 60°C for 5hr.



**Fig.14:** Synthetic Scheme of MoS<sub>2</sub>

### 3.4 Synthesis of Ternary Composite MoS<sub>2</sub>/Bi<sub>2</sub>O<sub>3</sub>/CdS

In a typical synthetic procedure, 22.6mg of as-prepared bismuth oxide, that was obtained after calcination, was finely grounded and added to precursors of Cadmium Sulfide. Cadmium acetate, 0.533g or 2mmol, was added to 60ml of ethylene diamine upon stirring followed by the addition of Thiourea, 0.448g or 2mmol. Then the as-prepared Bi<sub>2</sub>O<sub>3</sub> yellow powder was added into the mixture solution, then 10.7mg of MoS<sub>2</sub>, i.e. 8% is added to the solution and the whole mixture solution is sonicated for 30mins to form a uniform dispersion. After that, the solution is poured into the steel autoclave that is Teflon lined, which is then placed in a heating oven for 105° C for a duration of 8hrs. After reaction's completion time, the green-colored product was taken out from the autoclave and washed thrice each with ultra-pure water followed by Ethanol and then dried in a vacuum oven at 60° C for 3 hours. The dried product obtained was ready for

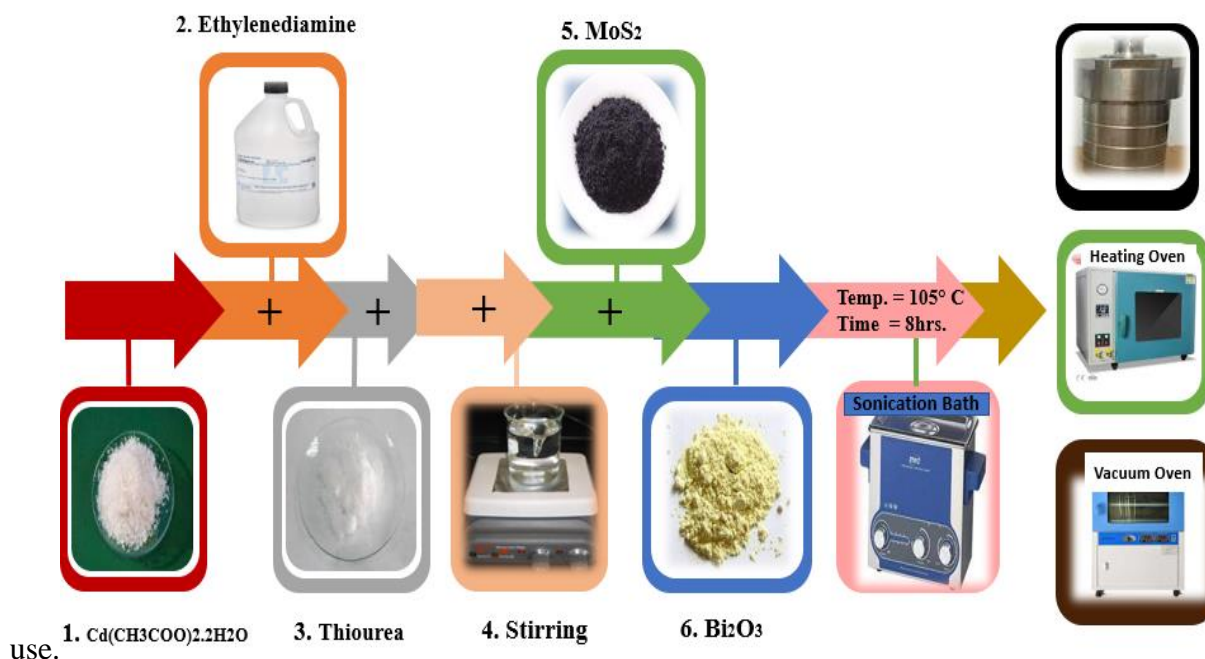


Fig.15: Synthetic Scheme of  $\text{MoS}_2/\text{Bi}_2\text{O}_3/\text{CdS}$

## Other Synthesis

$\text{BiVO}_4$  nanosheets can be prepared by adopting the following procedure;

Anhydrous Bismuth Nitrate is used as a Bismuth source while Ammonium metavanadate as a Vanadium source. For synthesis of  $\text{BiVO}_4$ , two solutions were made; Solution-1 contains 2mmol (0.789g) of Anhydrous Bismuth Nitrate dissolved in 40ml of Ethylene Glycol and solution-2 contains 2mmol (0.233g) of Ammonium meta-vandate dissolved in 40ml of lukewarm DI water. Both solutions were stirred for 30mins and then solution-2 was added dropwise into solution-1 upon stirring and a prominent color change (transparent to orange) is visualized. The mixture solution was vigorously stirred for 30mins to make a homogenous solution. Then, it was poured in 100ml Teflon steel-lined autoclave so that the Teflon was filled to  $\frac{3}{4}$ <sup>th</sup> of it,  $\frac{1}{4}$ <sup>th</sup> part of Teflon must be vacant to create autogenous pressure during the reaction. The autoclave was placed in heating oven at 100°C for a time period of 12hrs. After the completion of reaction, green color solution was formed which was centrifuged at 8000rpm for 8mins. The final product undergoes washing with DI water thrice to eliminate any inorganic impurities and finally washed



thrice with commercial ethanol at 8000rpm for duration of 8mins using the centrifugation machine. For drying, the resultant product was poured in petri-dish and placed in vacuum oven at 80° C for 3-4 hours.

### **Synthesis of Graphitic Carbonitride:**

Few layered graphitic Carbonitride was synthesized by a one-pot calcination process by using equal masses of both precursors; urea and melamine.

1. In a simple process, 4.5g of Urea and 4.5g of Melamine are finely grounded and taken in a 30ml crucible made of alumina that is covered with its lid so that it gets half-filled.
2. It is then calcined under Argon and air atmosphere in a chamber furnace at 550 degrees Celsius for 4hr at a heating rate of 2.3 °C/min while the ramping time is set to be 239mins. At this high temperature, CO<sub>2</sub> and NH<sub>3</sub> gases get evolved and intercalation occurs into layers of g-C<sub>3</sub>N<sub>4</sub>. Here, urea being a supplementary material undergoes complete decomposition at high temperature. i.e. 550° C and assist in the formation of layered graphitic carbonitride.

## Chapter 4

### Results and Discussion

#### 4.1 X-ray Diffraction (XRD)

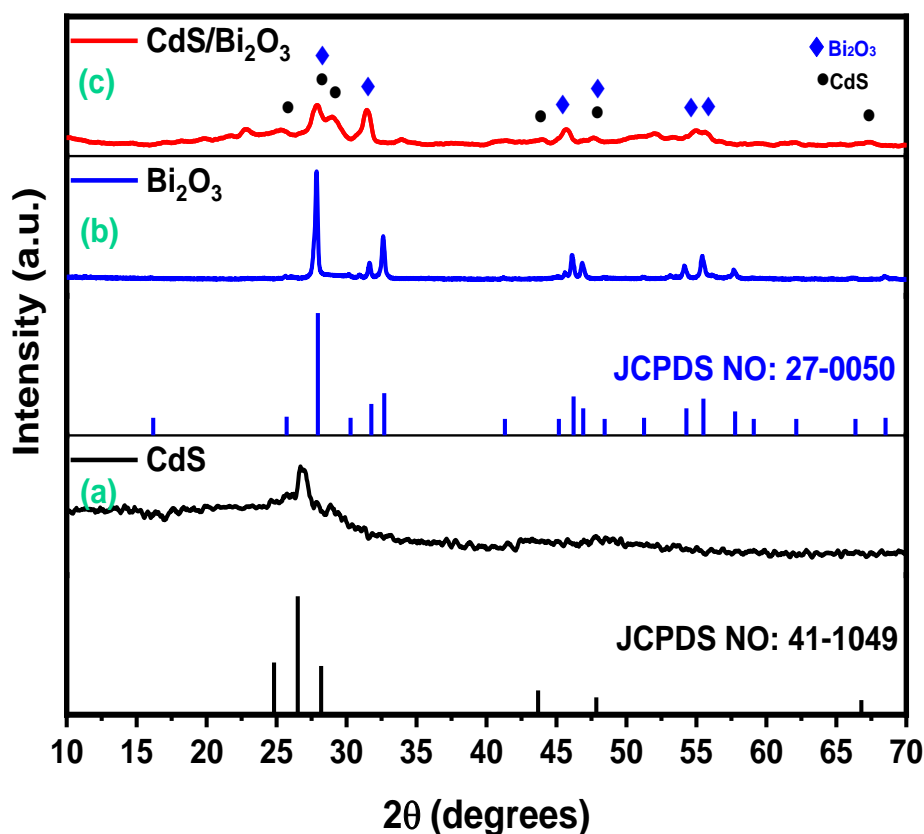


**Fig.16:** Diffraction pattern of (a) CdS (b)  $\text{Bi}_2\text{O}_3$  (c)  $\text{Bi}_2\text{O}_3/\text{CdS}$  in XRD

X-ray diffraction analysis of photocatalysts was performed. Fig (a) shows the diffraction pattern of Cadmium Sulfide has a hexagonal phase preferentially that matches well with the reported data in JCPDS card no 41-1049 for CdS ( $a = 4.1409 \text{ \AA}$ ,  $b = 4.1409 \text{ \AA}$ ,  $c = 6.7198 \text{ \AA}$ ). There were no characteristic peaks observed for CdO or C, showing that the material is pure CdS nanosheets. Fig(a) has 3 main peaks centered at  $2\theta$  values of 24.45, 26.65, and 28.75 corresponding to the hkl values of (100), (002), and (101) respectively. The peaks at  $2\theta$  values of 43.65, 47.8, and 66.5 correspond to (110), (103), and (203) planes respectively. The obtained results confirm the formation of hexagonal Cadmium Sulfide nanosheets prepared via a hydrothermal method.

Fig (b) shows the XRD pattern of as-synthesized highly crystalline Bismuth oxide. The peaks indexed at 25.56, 27.7, and 32.7 correspond purely to the monoclinic phase of Bi<sub>2</sub>O<sub>3</sub> (210), (201), and (220) crystal planes respectively. The sharpness and intensity of diffraction peaks show that the Bi<sub>2</sub>O<sub>3</sub> is crystalline in nature. The distinct diffraction peaks indexed at 2θ value of 41.2, 45.02, 46.16, 46.84, 48.4, 51.26, 54.07, 55.42, 57.64 refers to (212), (321), (222), (400), (410), (411), (203), (421), (402) crystal planes respectively match well with the reference pattern in JCPDS card no 27-0050. Debye Scherer's formula helps calculate the size of nanoparticles.

$$D = 0.94\lambda/\beta\cos\theta$$

k = Scherrer's constant and its value is very close to unity, i.e. 0.94 but varies with the crystallite shape.

λ = Wavelength of used x-rays (Cu k-α are commonly used with a wavelength of 0.15405 nm)  
 β = Full-width half maximum (FWHM) of the peak observed

θ = Angle of Diffraction

Fig© shows the xrd spectrum of CdS/Bi<sub>2</sub>O<sub>3</sub> and all the characteristic peaks of CdS and Bi<sub>2</sub>O<sub>3</sub> are present in it. The successful doping of 10% Bi<sub>2</sub>O<sub>3</sub> nanoparticles over CdS was confirmed due to the presence of common peaks in the nanocomposite but with less intensity. Due to the distortion of a lattice, the loss of crystallinity is observed in the nanocomposite CdS@Bi<sub>2</sub>O<sub>3</sub> thus, broadened peaks have been observed as compared to pure materials. No chemical interaction is found between Bi<sub>2</sub>O<sub>3</sub> and CdS since the diffraction peaks of both the pure materials are present in the composite, and no diffraction pattern for impurities is observed. This is an indication that a cohesive composite material is formed by the combination of Bi<sub>2</sub>O<sub>3</sub> and CdS. Moreover, the secondary peaks are absent which confirms that the nanocomposite is pure.

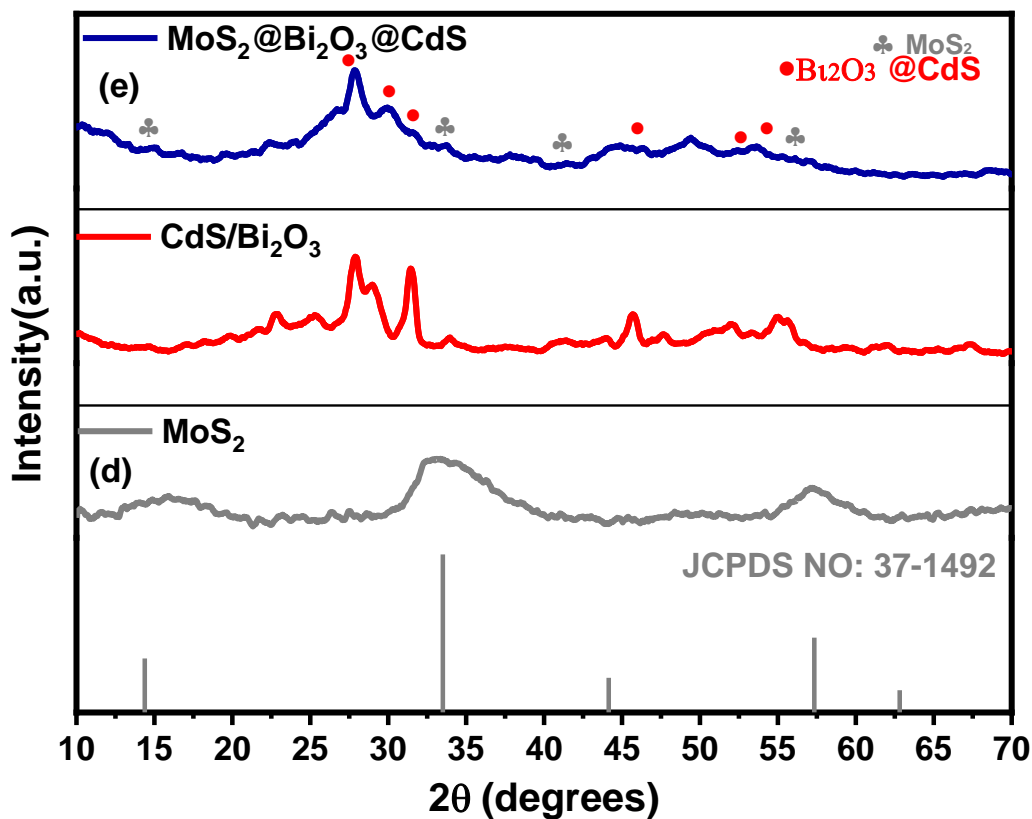


Fig.17: XRD pattern of (d) MoS<sub>2</sub>, (e) MoS<sub>2</sub>/Bi<sub>2</sub>O<sub>3</sub>/CdS

The X-ray diffraction pattern of MoS<sub>2</sub> is shown in Fig(d). The spectrum shows that most of the intensity integrated in it refers to a broad peak of amorphous substance, while the (002) peak indexed at 14.37 which refers to the crystalline MoS<sub>2</sub> is not much intense showing the less crystalline nature of MoS<sub>2</sub>. This indicates that MoS<sub>2</sub> layers are less stacked and packing is highly disordered. The as-synthesized MoS<sub>2</sub> nanospheres are hexagonal in phase and belong to the space group P63/mmc. The crystal planes (100), (006), (110), (107) corresponds to the 2θ values of 32.45, 44.15, 57.38, and 62.81 respectively that are well aligned with the JCPDS card no 37-1492. Fig(e) shows the x-ray diffraction pattern of ternary nanoheterojunction, 6% doped CdS/Bi<sub>2</sub>O<sub>3</sub>. The diffraction pattern contains the characteristic peaks of hexagonal MoS<sub>2</sub> as well as that of binary nanocomposite CdS/Bi<sub>2</sub>O<sub>3</sub> with slight shifting and reduction in the intensity of peaks. This confirms the successful development of interface between the pure materials. The

crystal structure of a material gives information about the optical and electrical properties of a material.

## 4.2 XPS

XPS is a characterization technique that gives information about the bonding states and chemical composition. The composite  $\text{Bi}_2\text{O}_3/\text{CdS}$  consists of Bi, S, Cd, and O. The O 1s peaks, gives information about the oxygen content of the material, are deconvoluted into a pair of symmetric peaks lying at a binding energy of 529 and 531eV that are attributed to the lattice oxygen and the chemisorbed oxygen respectively. Bi shows 2 characteristic peaks that determine the oxidation state of Bismuth. The lower energy peak centered at 158eV is ascribed to Bi  $4f_{7/2}$  while the higher energy peak centered at 163eV corresponds to Bi  $4f_{5/2}$  respectively which confirms the oxidation state of Bi to be +3. The peaks emerging at a binding energy of 160.78eV and 161.7eV were attributed to S  $2p_{3/2}$  and S  $2p_{1/2}$  respectively suggesting the oxidation state of Sulphur to be -2 in the product. Whereas, S 2s deconvoluted into 2 peaks, a lower energy peak centered at 225eV and a higher energy peak centered at 231eV corresponding to S  $2s_{3/2}$  and S  $2s_{1/2}$  orbitals of divalent sulfide ions. The XPS spectrum of Cd 3d in  $\text{Bi}_2\text{O}_3/\text{CdS}$  shows 2 high intensity peaks that corresponds to Cadmium atoms present in Cd-S bonds centered at 404eV and 411eV that are attributed to Cd  $3d_{5/2}$  and Cd  $3d_{3/2}$  respectively. The interpretation of these XPS peaks provides valuable insights into the chemical interactions of Bismuth with other elements present in the nanocomposite as well as gives information about the electronic structure of the composite. It is useful in understanding the interface properties, surface chemistry, catalysis and energy conversion.

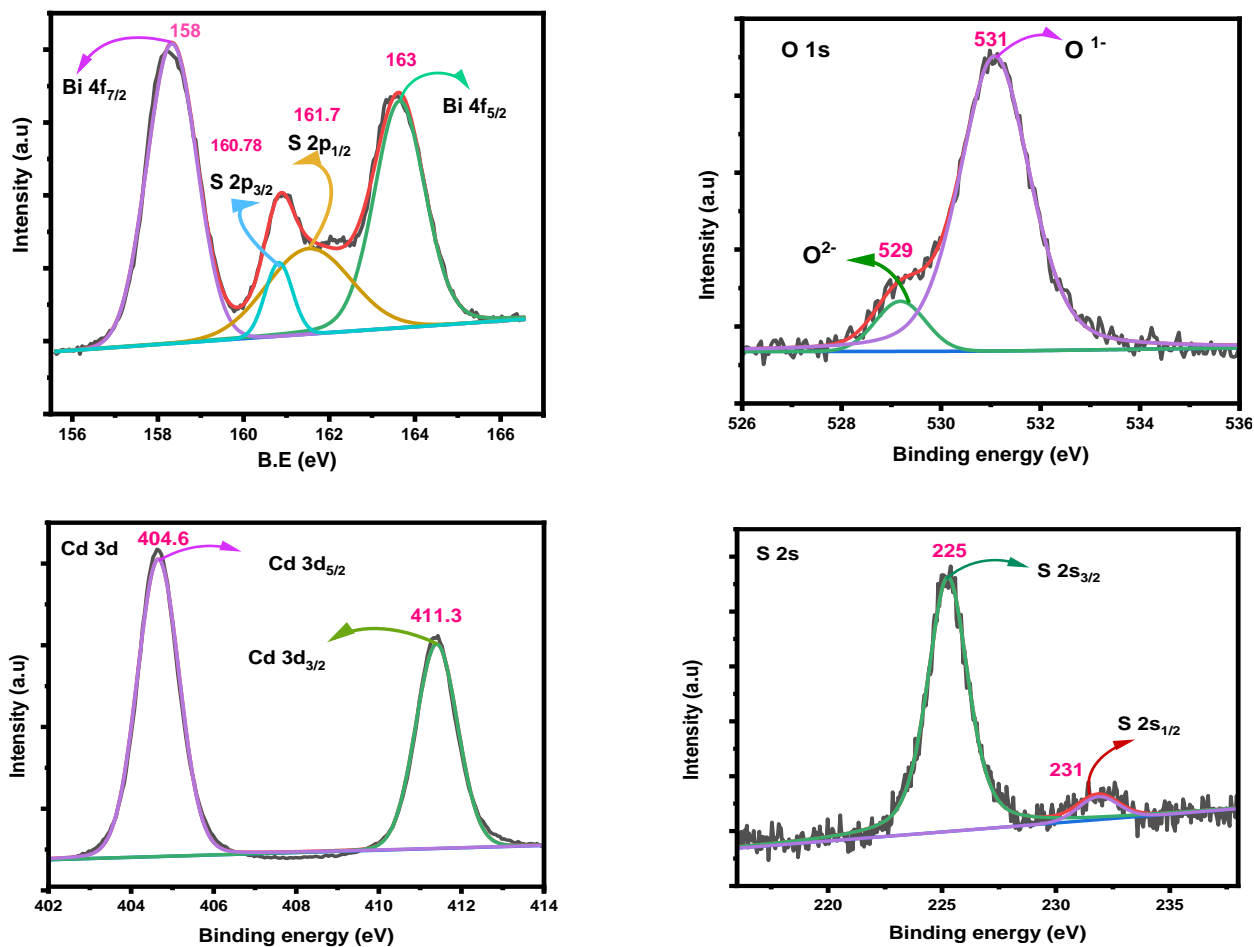


Fig.18: XPS spectrum of Bi<sub>2</sub>O<sub>3</sub>/CdS

### MoS<sub>2</sub>/Bi<sub>2</sub>O<sub>3</sub>/CdS

The XPS spectrum of the ternary composite shows the O 1s is deconvoluted into 2 peaks at 530.5eV and 532.4eV corresponding to divalent and monovalent anionic oxygen. Bi 4f shows 2 peaks, at 159eV and 164eV attributing to Bi 4f<sub>7/2</sub> and Bi 4f<sub>5/2</sub> with a slight shifting in peak positions as compared to Bi 4f in Bi<sub>2</sub>O<sub>3</sub>/CdS indicating the successful formation of ternary heterojunction. S 2p shows 2 peaks centered at 162eV, and 163eV attributing to S 2p<sub>3/2</sub> and S 2p<sub>1/2</sub> respectively. The XPS spectrum of ternary composite shows doublet of peaks for Mo 3d centered at 225eV and 231eV corresponding to Mo 3d<sub>5/2</sub> and Mo 3d<sub>3/2</sub> indicating the +4-oxidation state of Mo.

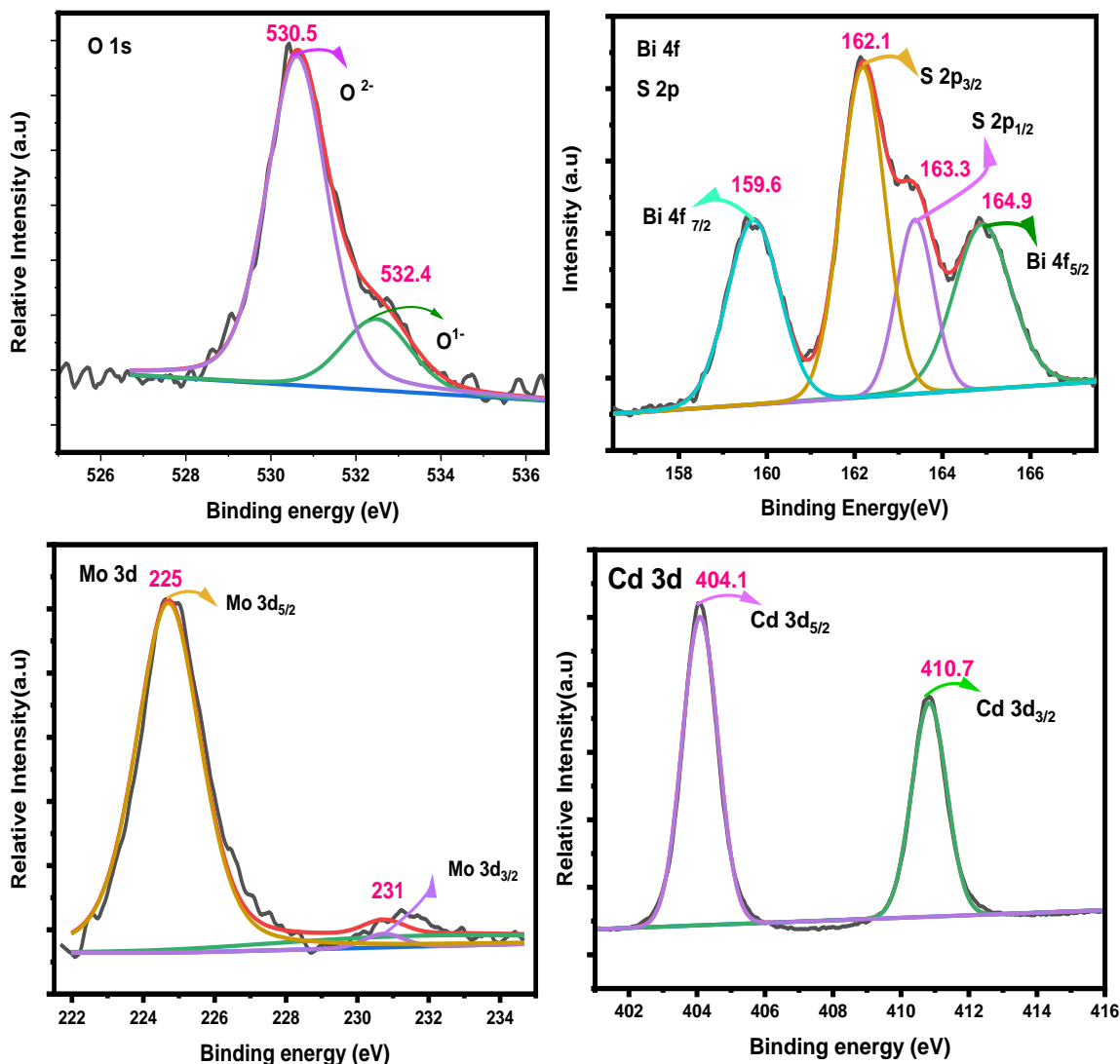


Fig.19: XPS spectrum of MoS<sub>2</sub>/CdS/Bi<sub>2</sub>O<sub>3</sub>

### 4.3 BET

BET is a technique that is used to measure a material's specific surface area. Bi<sub>2</sub>O<sub>3</sub>/CdS binary nanocomposite is composed of CdS nanoparticles that are uniformly dispersed in a matrix of Bi<sub>2</sub>O<sub>3</sub>. CdS is involved in the enhancement of optical and photocatalytic properties of the nanocomposite. Specific surface area in case of composite refers to the total surface area and composites are formed to increase the surface area thus having more active sites for the photocatalytic chemical reactions. The specific surface of composites is greater than the pure or individual components. It is because when a composite is formed, binary or ternary, the

individual components have varying morphology and surface roughness that fits into the pores and irregularities of other material making a interconnected surface. This is called interlocking effect and is responsible for increment in the overall surface area of the nanocomposite. Another factor may be the synergistic effect which refers to the increase in the specific surface area of the composite because one component enhances the porosity of the other. The quantification of specific surface area aids researchers to be aware of the effectiveness and efficiency of Bi<sub>2</sub>O<sub>3</sub>/CdS and MoS<sub>2</sub>/Bi<sub>2</sub>O<sub>3</sub>/CdS nanocomposite in applications such as sensors, solar cells, and photocatalysis.

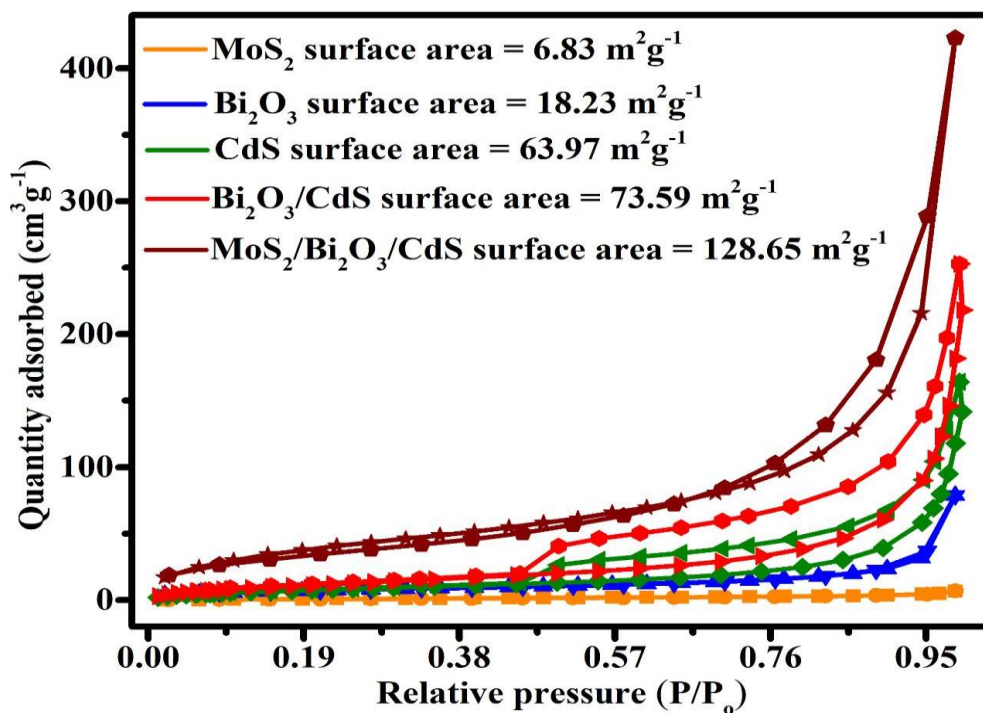


Fig.20: BET of MoS<sub>2</sub>, CdS, Bi<sub>2</sub>O<sub>3</sub>, Bi<sub>2</sub>O<sub>3</sub>/CdS, MoS<sub>2</sub>/Bi<sub>2</sub>O<sub>3</sub>/CdS

#### 4.4 SEM

CdS, Bi<sub>2</sub>O<sub>3</sub>, and MoS<sub>2</sub> are the semi-conducting materials that possess distinct morphologies. Cadmium Sulfide possess two-dimensional flower like structure owing to its high flexibility and thin nanosheets making up the crystal lattice. Such crystal structure of CdS is termed as hexagonal wurtzite resulting in flexible and thin nanosheets along the planes of a crystal. The synthesized Bi<sub>2</sub>O<sub>3</sub> possess ultra-thin tiny 2-D crystals called nano-flakes making



clusters together. The morphological studies of as-prepared samples were performed by SEM. Figure(a) reveals the sheet like structure of CdS with smooth and clean surface. Fig(b) shows the highly crystalline nanoflakes of Bi<sub>2</sub>O<sub>3</sub> formed by hydrothermal method followed by calcination. Fig(c) shows the nanospheres of MoS<sub>2</sub>. Fig(d) reveals the successful distribution of Bi<sub>2</sub>O<sub>3</sub> nanoflakes over CdS nanosheets thus results in the formation of interfacial heterostructure. Fig(e,f) shows the uniform distribution of MoS<sub>2</sub> nanospheres on the surface of CdS/Bi<sub>2</sub>O<sub>3</sub> binary nanoheterojunction, thus leads to the effective development of ternary interfacial heterojunction.

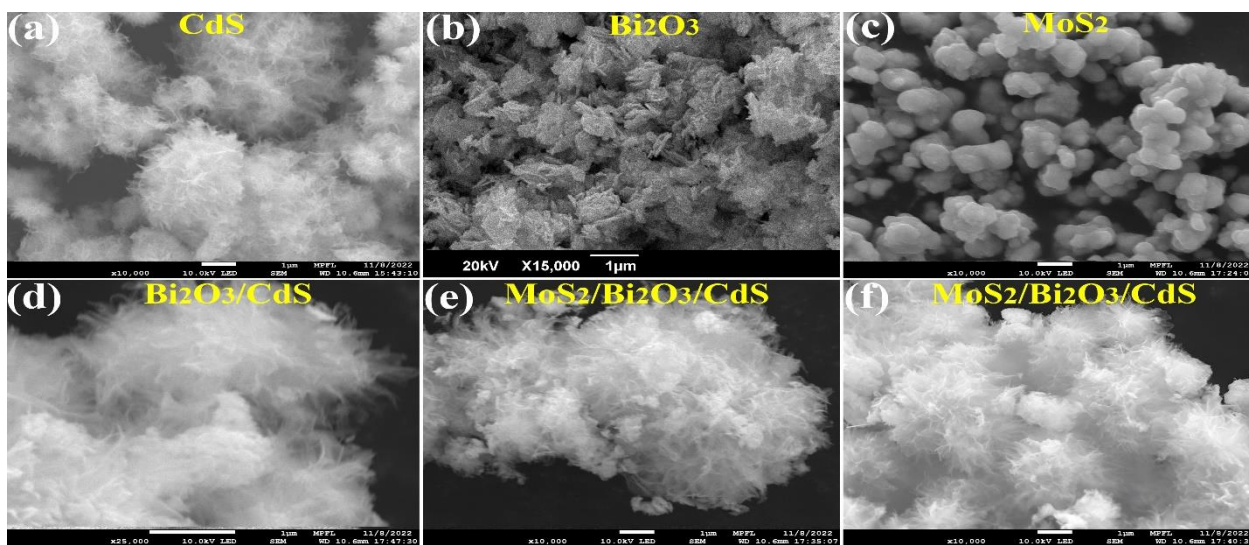


**Fig.21:** SEM images of different photocatalysts

#### 4.5 EDX

At nanoscale, the purity and compositional analyses were performed using EDX. The percentage composition by atomic weight and the compositional elements of Cadmium Sulfide are given as the insets of Fig(22). Whereas  $K\alpha$ ,  $L\alpha$ ,  $M\alpha$  refers to x-rays emitted as a result of de-excitation from various shells. When a L-shell electron is de-excited to K-shell, the energy released or x-ray emitted is called  $K\alpha$ . When an electron jumps from M-shell to L-shell, the x-ray emitted is called  $L\alpha$ . When an electron is de-excited from N-shell to M-shell, the characteristic energy emitted is called  $M\alpha$ . Since Cadmium and Sulphur are present in equal proportion in CdS and the EDX spectrum shows approx the same ratio of both.

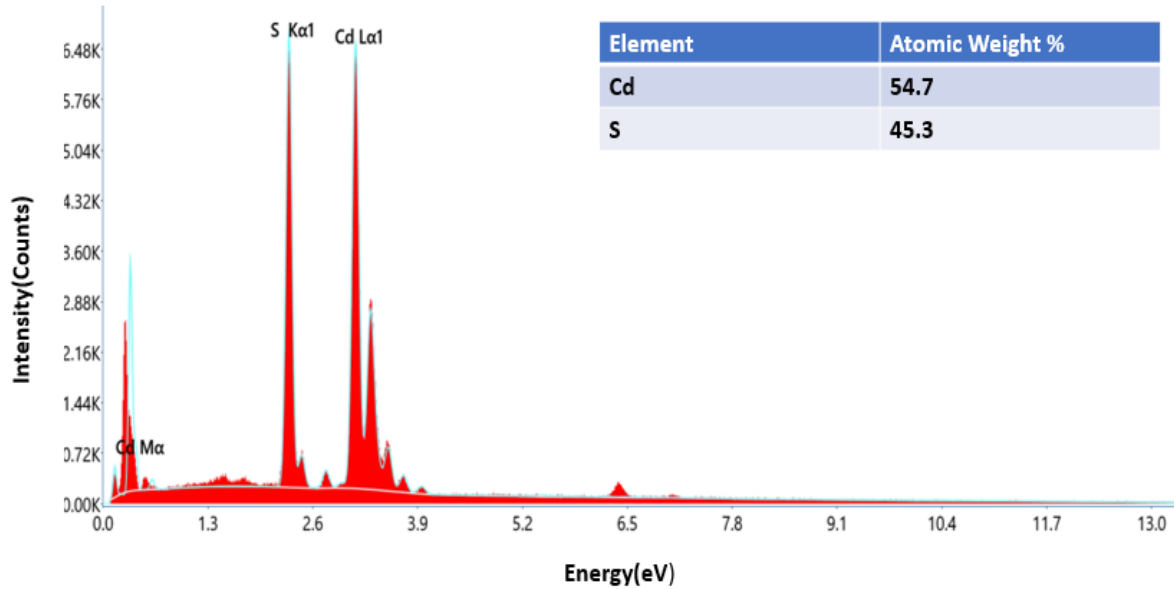


Fig.22: EDX spectrum of Cadmium Sulfide

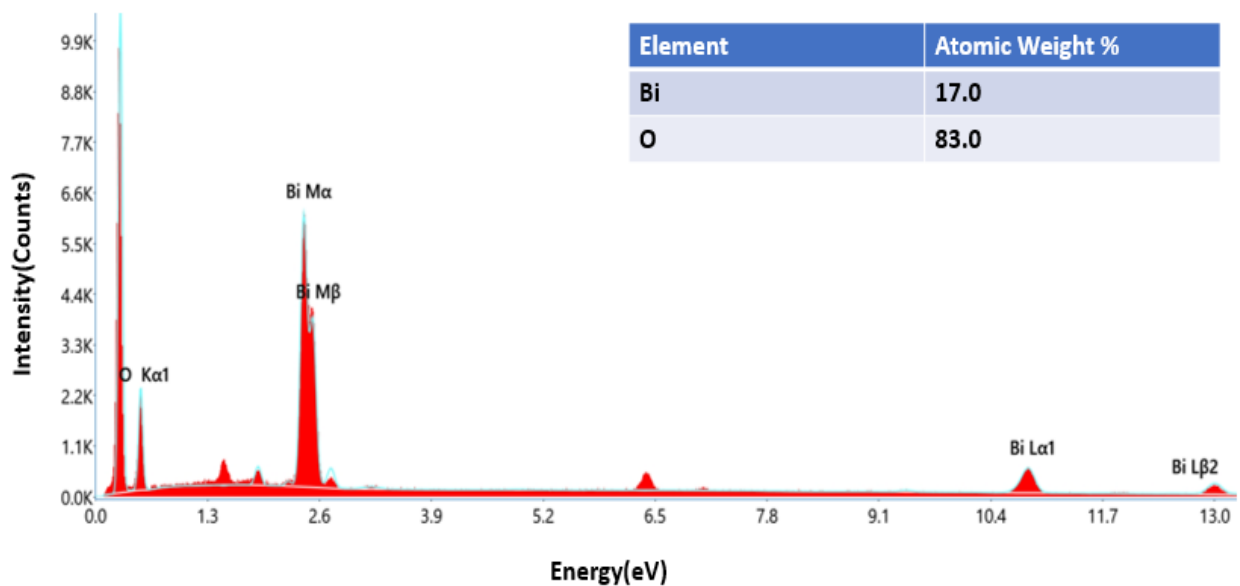
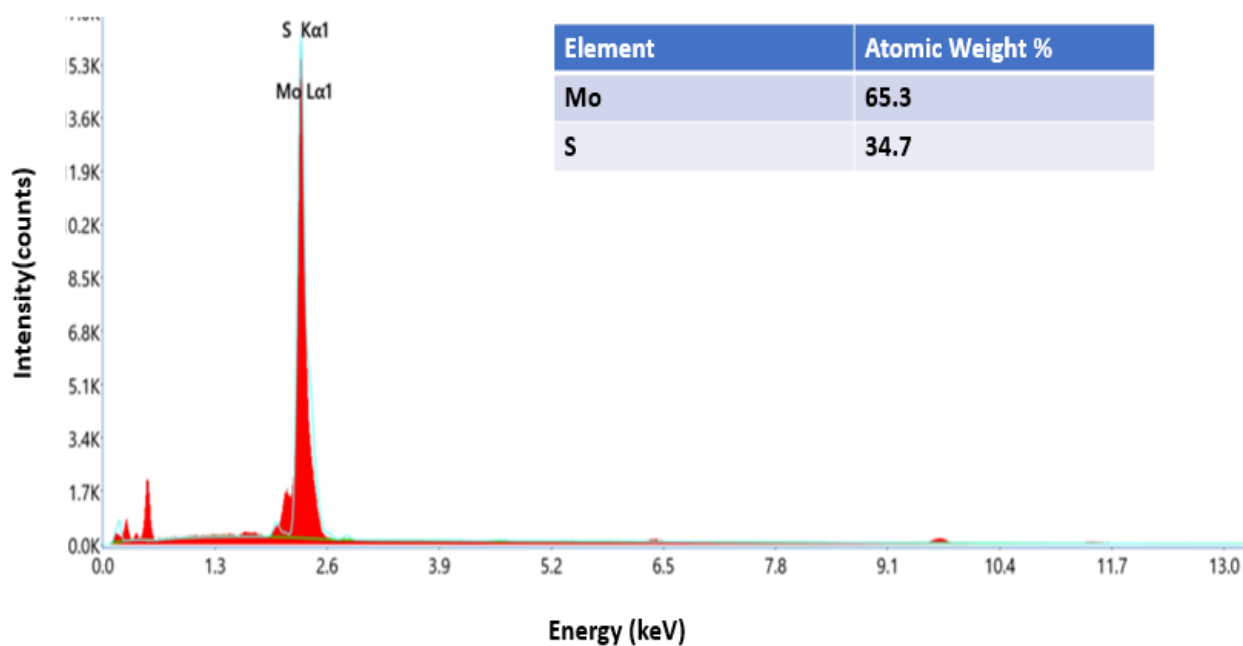


Fig.23: EDX spectrum of Bi<sub>2</sub>O<sub>3</sub>

Bismuth oxide is comprised of two elements Bi and O. The Atomic weight % of respective elements is shown as the insets of Fig(23 ).Whereas O K $\alpha$  refers to the de-excitation of electrons from L-shell to K-shell while M $\alpha$  and M $\beta$  refers to the electronic de-excitation from N-shell and O-shell respectively.



**Fig.24:** The EDX spectrum of MoS<sub>2</sub>.

The spectrum shows that the as-synthesized MoS<sub>2</sub> is comprised of two constituent elements; Mo and S and their atomic weight % are mentioned as the insets of Fig-24.

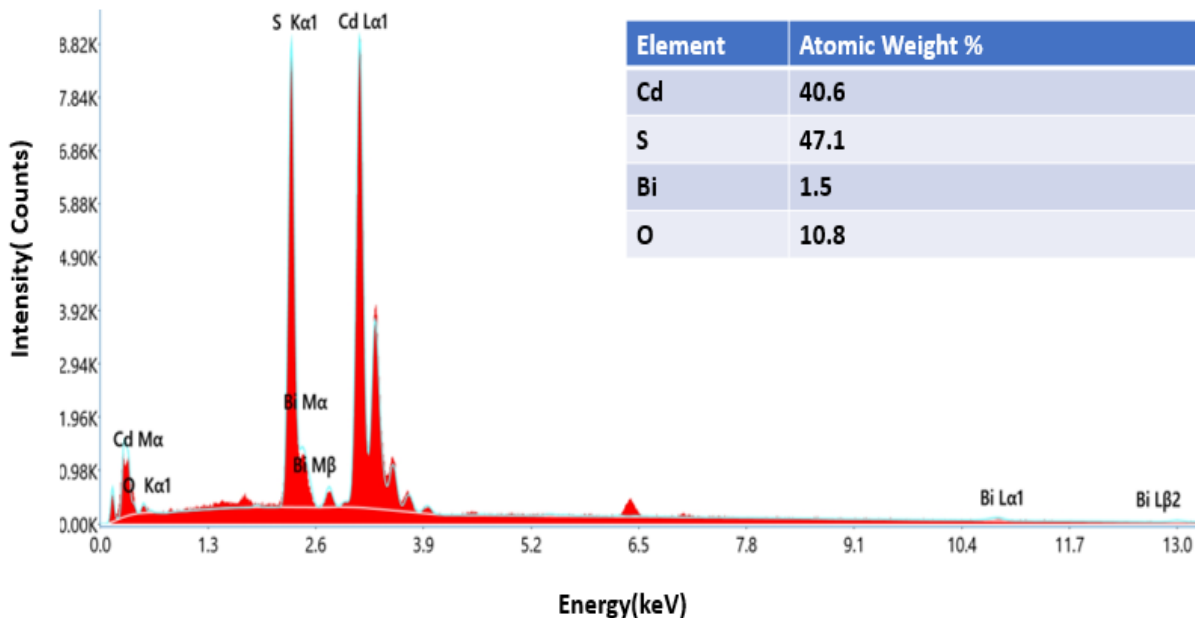


**Fig.25:** EDX spectrum of CdS/Bi<sub>2</sub>O<sub>3</sub>

EDX analysis supports TEM imaging and confirms the presence of all the constituent elements in the binary composite CdS/Bi<sub>2</sub>O<sub>3</sub> and their atomic weight %ages are mentioned as the insets in fig.25. In this spectrum, the peaks labeled as Cd -L and Cd-M indicates that Cadmium

is present in the composite. Whereas the peaks labeled as Bi M $\alpha$ , Bi M $\beta$ , Bi L $\alpha$ , Bi L $\beta$  ensure the presence of Bi in the composite. The peaks S-K $\alpha$  and O-K $\alpha$  indicate the presence of Sulphur and Oxygen in the composite. Thus, the EDX spectrum of the binary composite supports TEM results.

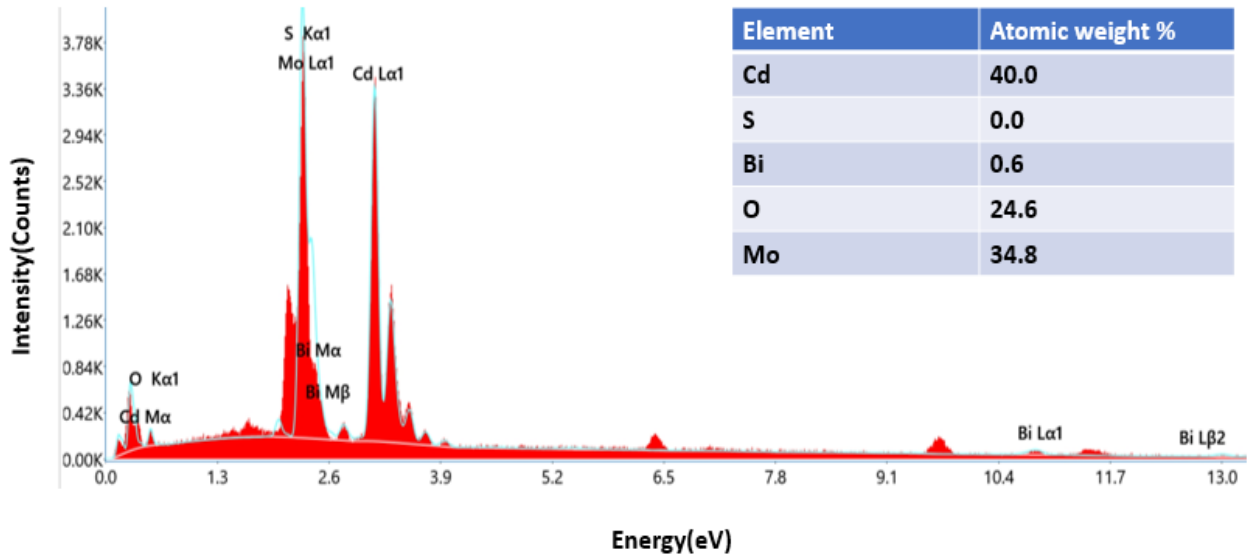


**Fig.26:** EDX spectrum of CdS/Bi<sub>2</sub>O<sub>3</sub>/MoS<sub>2</sub>

It can be seen that all the constituent elements are present in the ternary heterojunction CdS/Bi<sub>2</sub>O<sub>3</sub>/MoS<sub>2</sub> showing the successful formation of heterojunction.

## 4.6 Elemental Mapping & TEM

The distribution of elements in space can be visualized via Elemental Mapping. The elemental mapping of CdS/Bi<sub>2</sub>O<sub>3</sub> nanocomposite shows the uniform distribution of elements Cadmium, Bismuth, Sulfur, Oxygen in the nanosheets which indicates that all the component elements are homogeneously dispersed and well mixed together. Similarly, the mapping of MoS<sub>2</sub>/Bi<sub>2</sub>O<sub>3</sub>/CdS shows that all the component elements; Cd, Bi, S, O, Mo are uniformly distributed in the ternary composite. When the active components are homogeneously distributed, it results in charge separation and energy transfer more efficiently and leading to optimal photocatalytic performance.

At the nanoscale, the morphology and crystal structure of Bi<sub>2</sub>O<sub>3</sub>/CdS and MoS<sub>2</sub>/Bi<sub>2</sub>O<sub>3</sub>/CdS can be visualized by TEM and HRTEM. TEM image of Bi<sub>2</sub>O<sub>3</sub>/CdS revealed that the composite has 2-D ultra-thin, highly flexible, almost transparent nanosheets. This is attributed to the dominating ratio of CdS nanosheets in the binary heterojunction. The thinness and high flexibility of these 2-D nanosheets along the crystallographic planes revealed that the cadmium Sulfide nanosheets are decorated with Bi<sub>2</sub>O<sub>3</sub> nanoflakes, forming the binary nano-heterojunction.



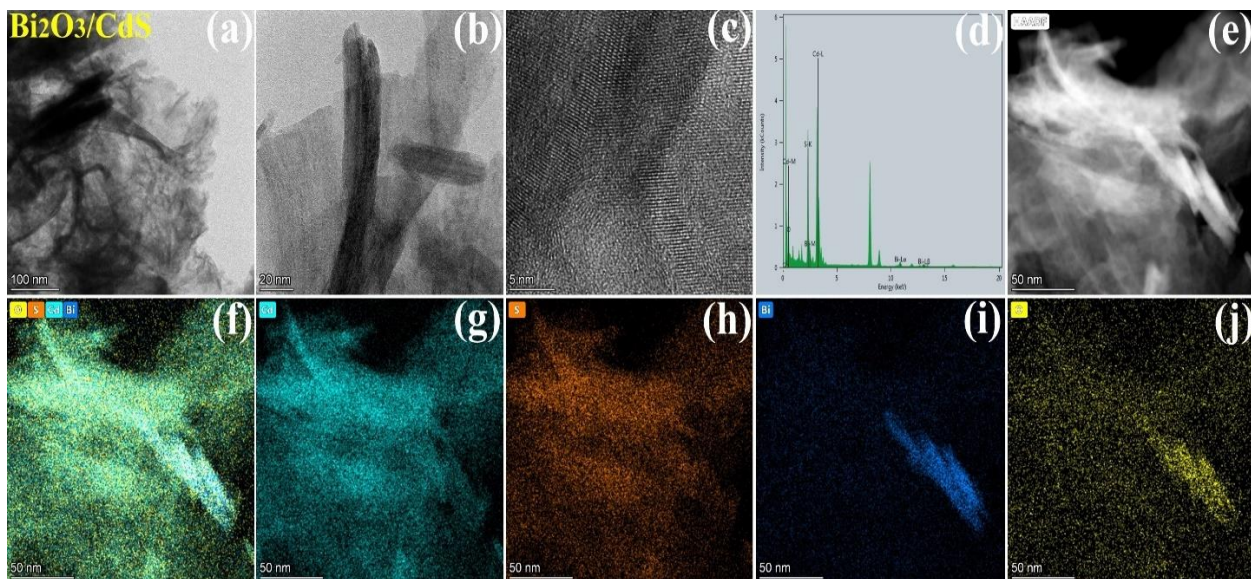


**Fig.27:** TEM and Elemental Mapping of CdS/Bi<sub>2</sub>O<sub>3</sub>

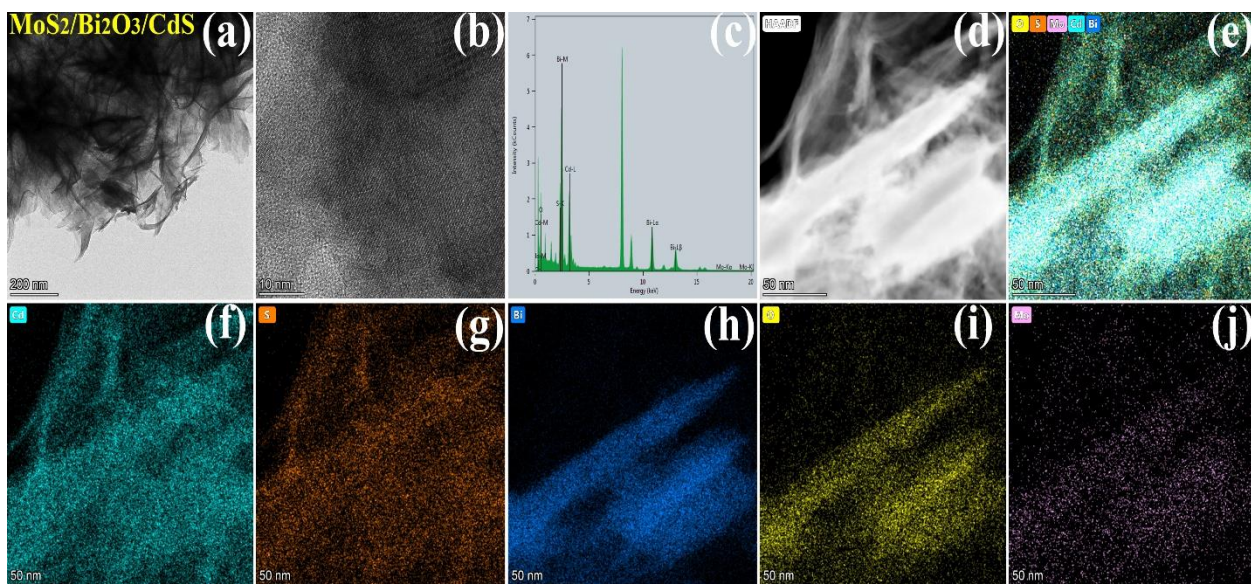


**Fig.28:** TEM and Elemental Mapping of MoS<sub>2</sub>/Bi<sub>2</sub>O<sub>3</sub>/CdS

#### 4.7 DRS

The electronic properties of semi-conductors can be determined by DRS by using the band gap of semi-conductor materials. Fig(29 ) is the Tauc plot that shows the direct bandgap of CdS by plotting the energy of photon on x-axis and  $(\alpha h\nu)^2$  on y-axis to be 2.5eV. The %age of reflected light is converted into Absorbance by Kubelka-Munk transformation. The bandgaps obtained by DRS are 3.2, 2.12, 2.46, 2.35eV for Bi<sub>2</sub>O<sub>3</sub>, MoS<sub>2</sub>, Bi<sub>2</sub>O<sub>3</sub>/CdS, MoS<sub>2</sub>/Bi<sub>2</sub>O<sub>3</sub>/CdS respectively. These bandgap values indicate that as the heterojunction or composite forms,

bandgap decreases owing to more absorption of the visible light by the composite thus, leading to a better catalyst for the photocatalytic applications.

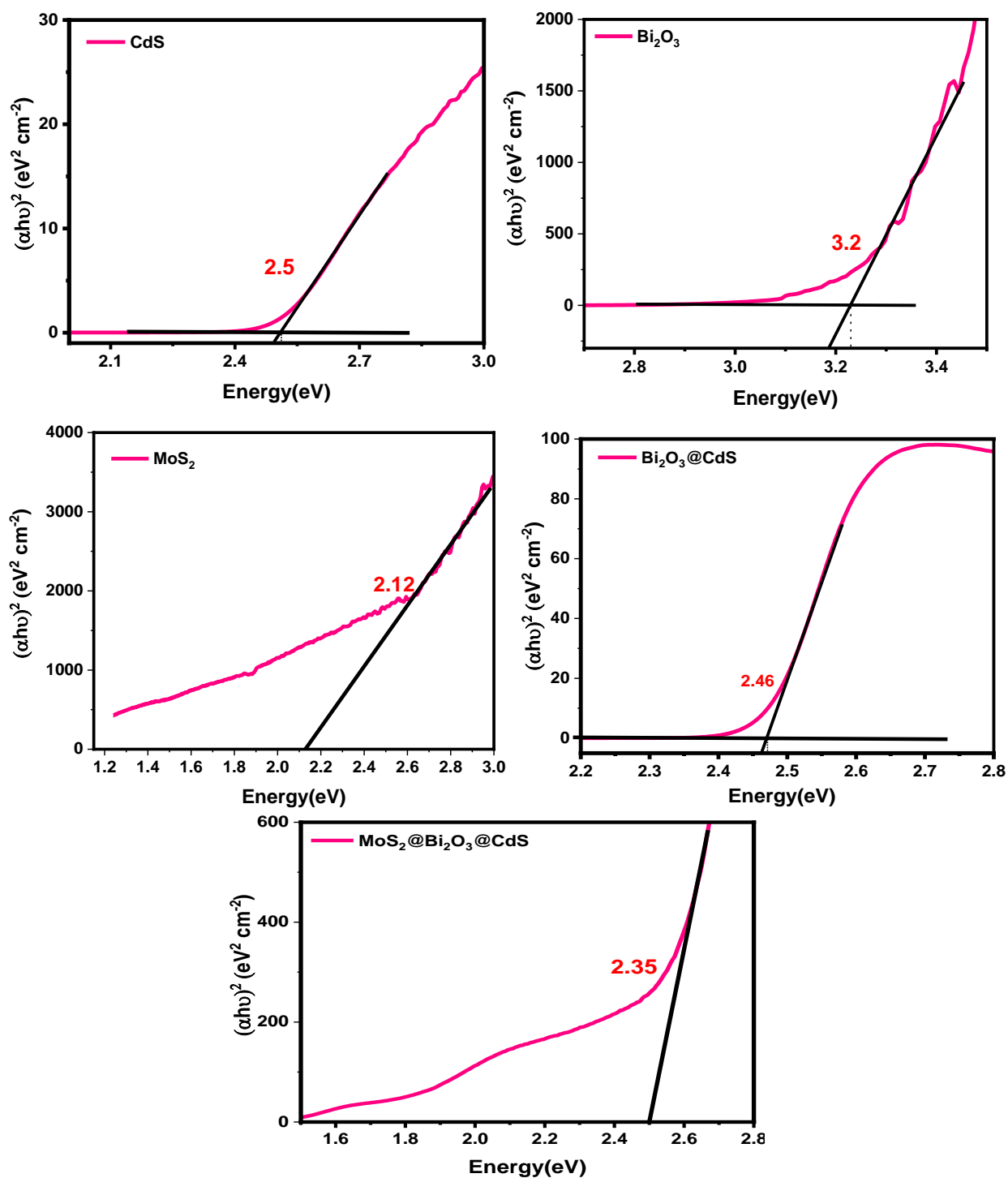


Fig.29:DRS analysis of the synthesized photocatalysts.

#### 4.8 Thermogravimetric Analysis

Cadmium Sulfide shows a weight loss of approx 10% upto 300°C that might be

attributed to the loss of moisture in the material. Then a further weight loss of 5% is observed upto 700°C that is due to loss of solvent residues. For Bi<sub>2</sub>O<sub>3</sub>, 8% weight loss occurs upto 400°C that may be attributed to the loss of moisture and any solvent residues but after that the material is stable till 800°C. For binary composite Bi<sub>2</sub>O<sub>3</sub>/CdS, a 12% weight loss is observed till 400°C due to loss of water molecules present then a further weight loss of 10% is observed till 800°C owing to the loss of solvent molecules. For MoS<sub>2</sub>, initially a weight loss of 3% is observed till 100°C then a sudden increase in weight loss occurs upto 350°C that are attributed to loss of moisture, solvent or any impurities. The ternary composite shows the initial weight loss of 7% till 300°C then a further weight loss of 4% is observed upto 500°C, again a very sharp increase in weight loss is observed till 800°C. Therefore, TGA is useful in determining the thermal stability of materials.

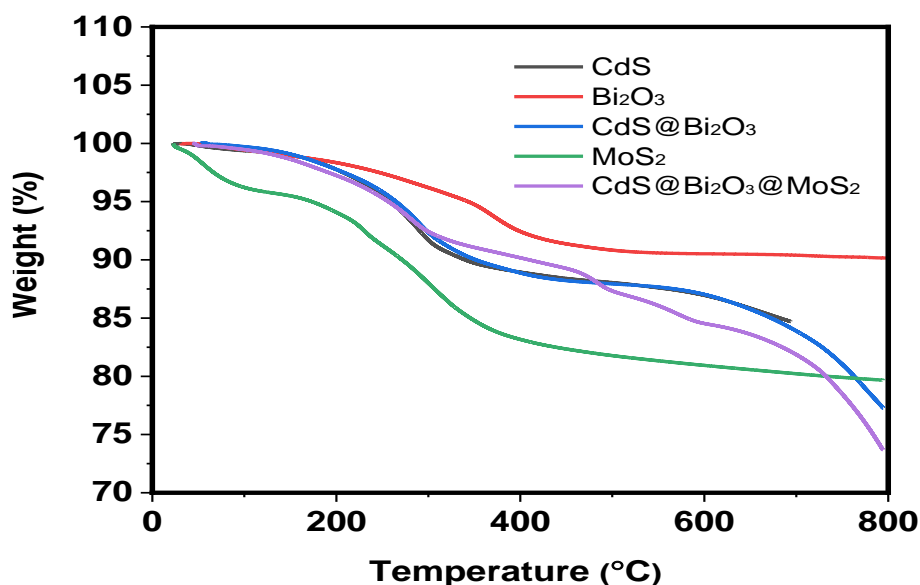


Fig.30: Thermogram of MoS<sub>2</sub>, CdS, Bi<sub>2</sub>O<sub>3</sub>, Bi<sub>2</sub>O<sub>3</sub>/CdS, MoS<sub>2</sub>/Bi<sub>2</sub>O<sub>3</sub>/CdS

### Catalyst Reusability

The reusability of the catalyst MoS<sub>2</sub>/Bi<sub>2</sub>O<sub>3</sub>/CdS was performed for 4 cycles. All showed remarkable stability up to approx 98%, indicating that the heterojunction catalyst is efficient enough for charge separation and can be reused. For the first cycle, the catalyst gave 99%



photodegradation efficiency. In the 2<sup>nd</sup> run, the catalyst gave 98.5% degradation efficiency. In 3<sup>rd</sup> cycle, the catalyst gave 98.8% degradation efficiency while in the 4<sup>th</sup> cycle, the photodegradation efficiency of the catalyst reaches 98%. The overall efficiency remained almost constant showing that the catalyst was stable up to 4 cycles.

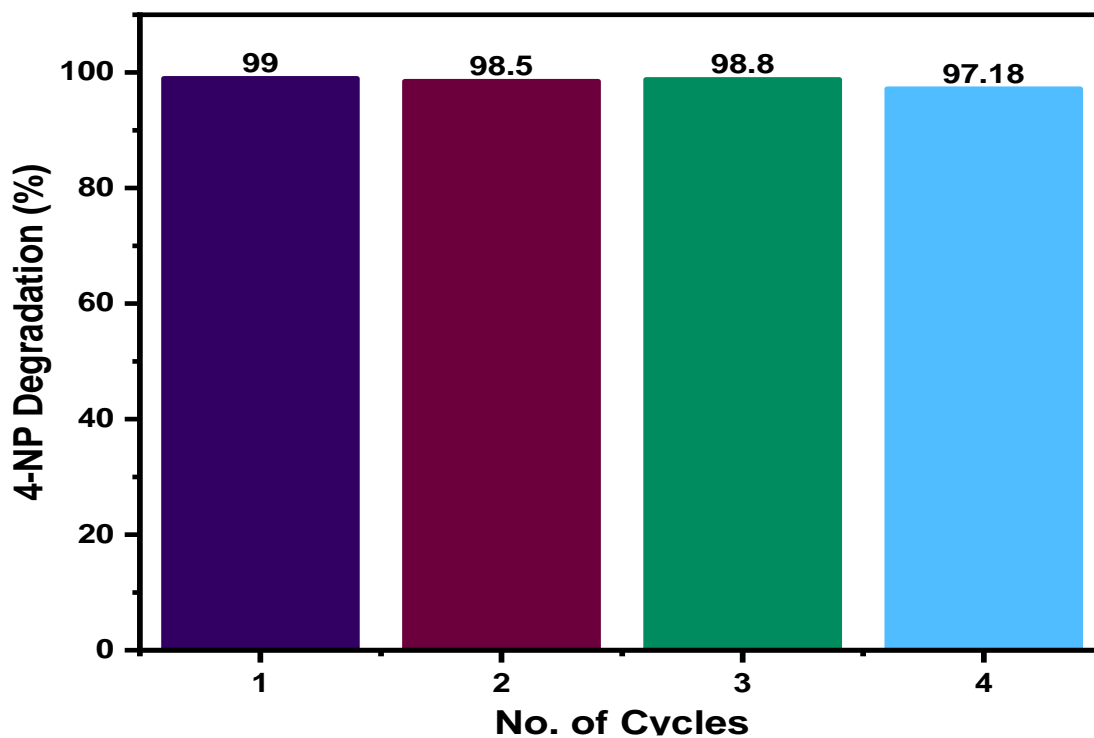


Fig.31: Bar Chart showing the Efficiency of photocatalyst in 4 cycles

### Photomineralisation Studies

The chemical process that involves the decomposition of organic pollutants into water and carbon dioxide by using the photocatalyst and a light source. This study entails the mineralization of 4-nitrophenol by using the as-synthesized photocatalysts CdS, Bi<sub>2</sub>O<sub>3</sub>, MoS<sub>2</sub>, Bi<sub>2</sub>O<sub>3</sub>/CdS, MoS<sub>2</sub>/Bi<sub>2</sub>O<sub>3</sub>/CdS. It was found that the composites showed better activity on photocatalysis compared to pure materials. This is due to the effective transfer and isolation of charge carriers between the components. The ROS, for-instance, radicals such as superoxide radical ( $O_2^{\bullet-}$ ) & hydroxyl radical ( $HO^{\bullet}$ ) are produced as primary oxidants during the reaction and serve for the mineralization of 4-nitrophenol. Upon degradation, the pollutant is not completely removed and it may be transformed to toxic byproducts. In this study, the potential of

MoS<sub>2</sub>/Bi<sub>2</sub>O<sub>3</sub>/CdS ternary composite as a promising photocatalyst for the efficient and effective removal of 4-nitrophenol, an organic pollutant, from wastewater has been highlighted.

### **Photodegradation of 4-nitrophenol**

The degradation studies of Bi<sub>2</sub>O<sub>3</sub>, CdS, MoS<sub>2</sub>, Bi<sub>2</sub>O<sub>3</sub>/CdS, MoS<sub>2</sub>/Bi<sub>2</sub>O<sub>3</sub>/CdS were performed and the photocatalytic removal of 4-nitrophenol was done by using 100ppm solution of 4-nitrophenol dye. Initially, a 1000ppm stock solution was prepared from which aliquots were taken to prepare 100ppm of the pollutant. The amount of catalyst that was added was 30 mg. Upon addition of 30mg of catalyst in 100ppm solution of 4-nitrophenol, it was stirred and then sonicated for 30mins to a uniform dispersion. After that, the solution was placed in the dark for 30 mins to establish adsorption-desorption equilibrium and aliquot was taken in the dark. Then, the solution was placed under constant stirring which was then exposed to the xenon lamp source. At regular intervals of 10 mins, the aliquots were subsequently taken and then analyzed by uv-vis spectrophotometer for pollutant removal or degradation.

The uv-vis absorption spectrum of CdS, Bi<sub>2</sub>O<sub>3</sub>, Bi<sub>2</sub>O<sub>3</sub>/CdS, MoS<sub>2</sub>/Bi<sub>2</sub>O<sub>3</sub>/CdS shows that pure 4-nitrophenol shows the phenolate ion peak in the dark that is of high intensity. The intensity of the phenolate ion peak was observed and it shows a continuous decrease with an increase in the time interval, indicating that the 4-nitrophenol is undergoing the degradation process in the presence of light source. For CdS, due to its photostability, it shows only the 50% degradation of 4-nitrophenol pollutant whereas the Bi<sub>2</sub>O<sub>3</sub> photocatalyst shows the removal % of 58 due to an increased rate of electron-hole recombination. The best photocatalytic activity was found for Bi<sub>2</sub>O<sub>3</sub>/CdS, as compared to pure photocatalysts, was 86% in 120 mins of light exposure which indicates the sufficient removal of pollutant. To further improve the efficiency of binary heterojunction, a ternary heterojunction MoS<sub>2</sub>/Bi<sub>2</sub>O<sub>3</sub>/CdS was synthesized that showed excellent degradation efficiency of 99% in 120 mins of light irradiation.

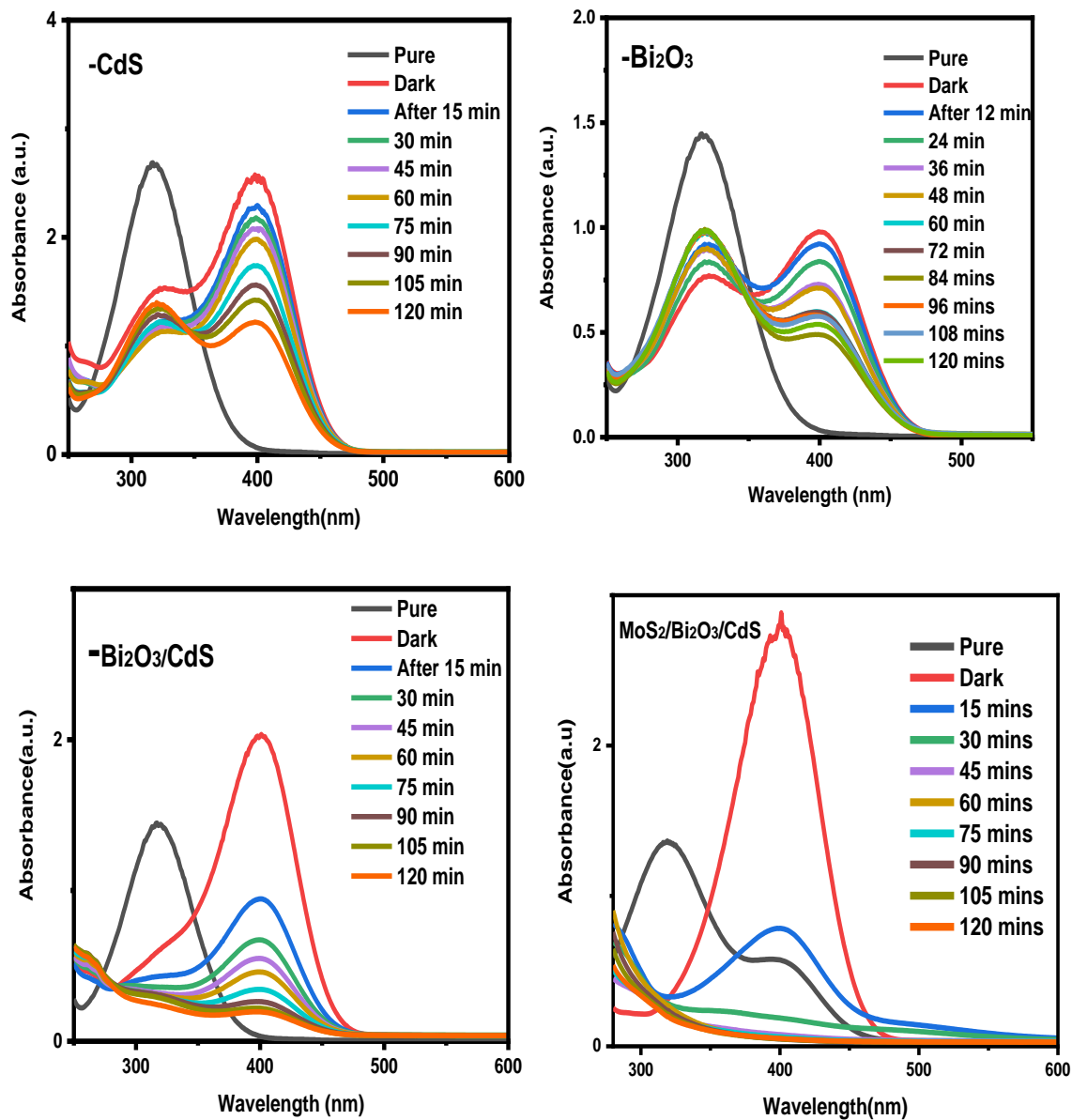


**Fig.32:** Uv-vis spectrum of Different photocatalysts( 30mg each in 100ppm pollutant solution)

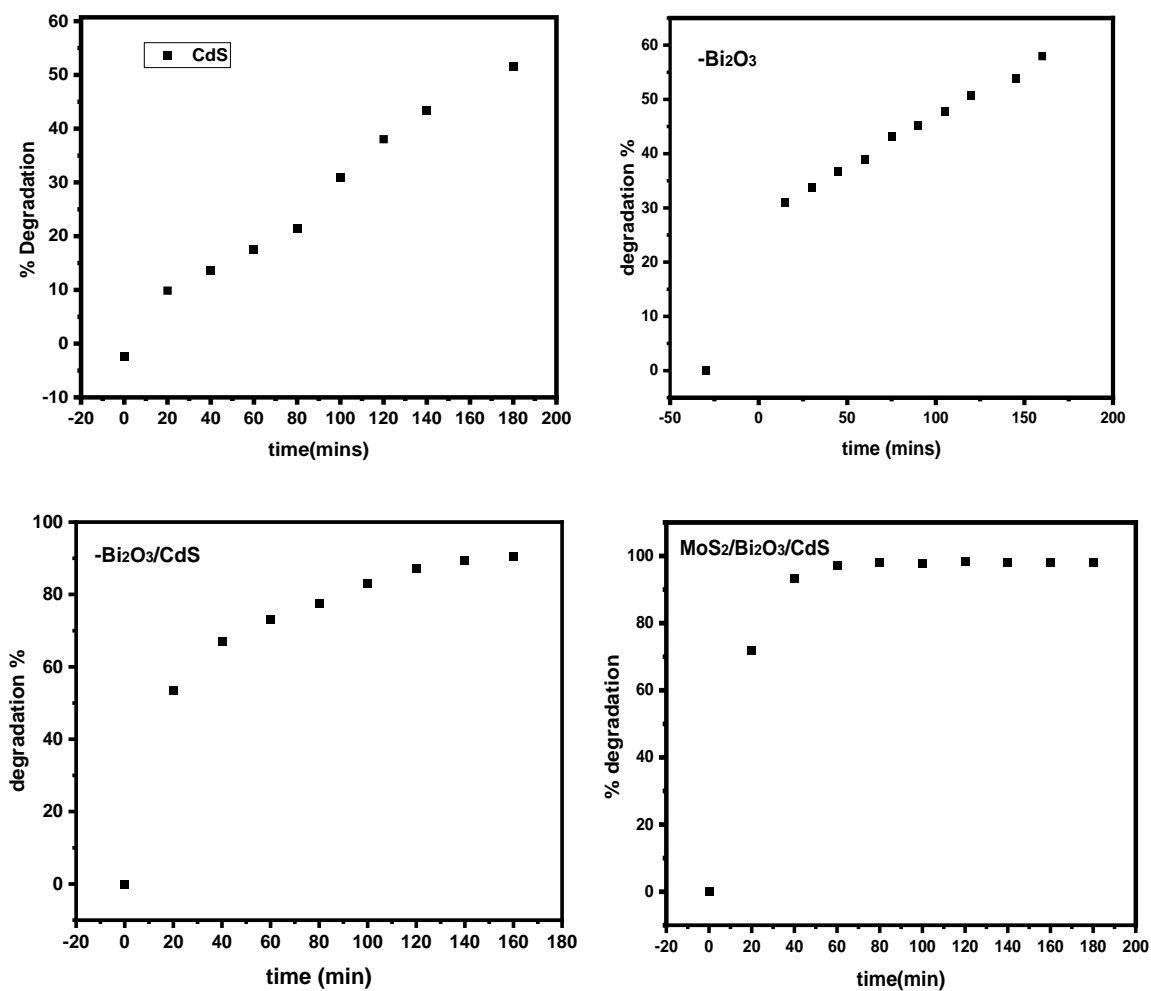


**Fig.33:** Graphs Showing % Degradation Efficiency of photocatalysts for 4-nitrophenol.

## Chapter 5

### Conclusion and Future Recommendations

The hydrothermal method was opted to synthesize novel semi-conductor photocatalysts heterojunction with its exceptional photocatalytic activity towards organic pollutant degradation. It was found that if the photogenerated-holes move quickly from CdS VB then it leads to the photocatalyst's stability. The charge transfer synergy between Bi<sub>2</sub>O<sub>3</sub>, CdS, MoS<sub>2</sub> leads to production of reactive oxygen species. The prepared materials were characterized by using XRD, SEM, HR-TEM, EDX, XPS, UV-VIS, Elemental Mapping, etc. The binary heterojunction synthesized showed good photocatalytic activity for 4-nitrophenol degradation and photo-mineralization was achieved up to 86% which was further improved by the ternary nano-heterojunction MoS<sub>2</sub>/Bi<sub>2</sub>O<sub>3</sub>/CdS that showed excellent activity with photo-mineralization of 99%. This S-Scheme 2-D ternary heterojunction was successfully synthesized with 99% removal of 4-nitrophenol for the first time. Future work may extend its applications to the supercapacitors and electrochemical water splitting and also the use of this ternary heterojunction to remove other organic/inorganic pollutants from waste water for water purification.

## References

- [1] M. Younger, H. R. Morrow-Almeida, S. M. Vindigni, and A. L. Dannenberg, "The built environment, climate change, and health: opportunities for co-benefits," *American journal of preventive medicine*, vol. 35, pp. 517-526, 2008.
- [2] Jeyaratnam, J.J.B.j.o.i.m., Health problems of pesticide usage in the Third World. 1985. 42(8): p. 505.
- [3 ] Kazi, T., et al., Assessment of water quality of polluted lake using multivariate statistical techniques: A case study. 2009. 72(2): p. 301-309
- [4 ] Regadío, M., et al., Containment and attenuating layers: An affordable strategy that preserves soil and water from landfill pollution. 2015. 46: p. 408-419.
- [5] Varavipour, M., T. Asadi, and M.J.R.O.C. Mashal, Application of two layers of soil with different textures for decreasing pollution from landfills to the subterranean water table. 2011. 12(3): p. 833-838.
- [6] Anju, A., et al., Water pollution with special reference to pesticide contamination in India. 2010. 2010.
- [7 ] Haines, A., et al., Climate change and human health: impacts, vulnerability and public health. 2006. 120(7): p. 585-596.
- [8] Mezzacapo, M., Donohue, M. J., Smith, C., El-Kadi, A., Falinski, K., & Lerner, D. T. (2020). Hawai 'i's Cesspool Problem: Review and Recommendations for Water Resources and Human Health. *Journal of Contemporary Water Research & Education*, 170(1), 35-75.
- [9] S. V. Kulkarni, C. Blackwell, A. Blackard, C. Stackhouse, and M. Alexander, *Textile dyes and dyeing equipment: classification, properties and environmental aspects*: US Government Printing Office, 1985.
- [10] C. Y. Lam, "Removal of crystal violet from aqueous solution using banana peel," UTAR, 2020.

- [11] E. J. Montes-Alba, G. de Jesús Camargo-Vargas, R. N. Agudelo-Valencia, and G. E. Dévora- Isiordia, "Adsorption Study of Acid Red 114 and Basic Blue 3 on Sunflower Stalk," *Journal of Water Resource and Protection*, vol. 11, p. 68, 2019.
- [12] A. Ajmal, I. Majeed, R. Malik, M. Iqbal, M. A. Nadeem, I. Hussain, *et al.*, "Photocatalytic degradation of textile dyes on Cu<sub>2</sub>O-CuO/TiO<sub>2</sub> anatase powders," *Journal of environmental chemical engineering*, vol. 4, pp. 2138-2146, 2016.
- [13] Vaiano, V., & De Marco, I. (2023). Removal of azo dyes from wastewater through heterogeneous photocatalysis and supercritical water oxidation. *Separations*, 10(4), 230.
- [14] A. Reife and H. S. Freeman, *Environmental chemistry of dyes and pigments*: John Wiley & Sons, 1996.
- [15] Hassaan, M., Advanced oxidation processes of some organic pollutants in fresh and seawater. *PhD, A Thesis, Faculty of Science, Port Said University* 2016.
- [16] Järup, L.J.B.m.b., Hazards of heavy metal contamination. 2003. 68(1): p. 167-182.
- [17] Zawierucha, I., et al., Immobilized materials for removal of toxic metal ions from surface/groundwaters and aqueous waste streams. 2016. 18(4): p. 429-444.
- [18] Longevialle, P. and O.J.O.m.s. Lefevre, Ion-neutral reorientation and unimolecular loss of alkanes from organic ions in the gas phase. 1993. 28(10): p. 1083-1086.
- [19] Yun, C.H., et al., Hollow fiber solvent extraction removal of toxic heavy metals from aqueous waste streams. 1993. 32(6): p. 1186-1195
- [20] Mohod, C.V., J.J.I.J.o.I.R.i.S. Dhote, Engineering, and Technology, Review of heavy metals in drinking water and their effect on human health. 2013. 2(7): p. 2992-2996.
- [21] Sigel, A. and H. Sigel, *Metal Ions in Biological Systems: Volume 34: Mercury and its Effects on Environment and Biology*. 1997: CRC Press.
- [22] Barakat, M.J.A.j.o.c., New trends in removing heavy metals from industrial wastewater. 2011. 4(4): p. 361-377.

- [23] Kenawy, I., et al., Adsorption of Cu (II), Cd (II), Hg (II), Pb (II) and Zn (II) from aqueous single metal solutions by guanyl-modified cellulose. 2018. 107: p. 1538-1549.
- [24] Haines, A., et al., Climate change and human health: impacts, vulnerability and public health. 2006. 120(7): p. 585-596.
- [25] Mekhilef, S., et al., A review on solar energy use in industries. 2011. 15(4): p. 1777-1790.
- [26] Wei, T.-Y.; Wang, Y.-Y.; Wan, C.-C., Photocatalytic oxidation of phenol in the presence of hydrogen peroxide and titanium dioxide powders. *Journal of Photochemistry and Photobiology A: Chemistry* **1990**, 55 (1), 115-126
- [27] Huang, A.; Cao, L.; Chen, J.; Spiess, F.-J.; Suib, S. L.; Obee, T. N.; Hay, S. O.; Freihaut, J. D., Photocatalytic degradation of triethylamine on titanium oxide thin films. *Journal of catalysis* **1999**, 188 (1), 40-47.
- [28] Dieckmann, M. S.; Gray, K. A., A comparison of the degradation of 4-nitrophenol via direct and sensitized photocatalysis in TiO<sub>2</sub> slurries. *Water Research* **1996**, 30 (5), 1169-1183.
- [29] Chen, D.; Ray, A. K., Photodegradation kinetics of 4-nitrophenol in TiO<sub>2</sub> suspension. *Water Research* **1998**, 32 (11), 3223-3234.
- [30] San, N.; Hatipoğlu, A.; Koçtürk, G.; Çınar, Z., Photocatalytic degradation of 4-nitrophenol in aqueous TiO<sub>2</sub> suspensions: theoretical prediction of the intermediates. *Journal of Photochemistry and Photobiology A: Chemistry* **2002**, 146 (3), 189-197.
- [31] Ameta, R.; Solanki, M. S.; Benjamin, S.; Ameta, S. C., Photocatalysis. In *Advanced oxidation processes for waste water treatment*, Elsevier: 2018; pp 135-175.
- [32] Wu, C.; Maurer, C.; Wang, Y.; Xue, S.; Davis, D. L., Water pollution and human health in China. *Environmental Health Perspectives* **1999**, 107 (4), 251-256.
- [33] Serpone, N. (2000). Photocatalysis. *Kirk-Othmer Encyclopedia of Chemical Technology*{Serpone, 2000 #185}
- [34] Wang, H.; Zhang, L.; Chen, Z.; Hu, J.; Li, S.; Wang, Z.; Liu, J.; Wang, X.,



Semiconductor heterojunction photocatalysts: design, construction, and photocatalytic performances. *Chemical Society Reviews* **2014**, *43* (15), 5234-5244.

[35] Zhang, K.; Guo, L., Metal sulphide semiconductors for photocatalytic hydrogen production. *Catalysis Science & Technology* **2013**, *3* (7), 1672-1690.

[36] Chen, F.; Zhou, R.; Yang, L.; Shi, M.; Wu, G.; Wang, M.; Chen, H., One-step fabrication of CdS nanorod arrays via solution chemistry. *The Journal of Physical Chemistry C* **2008**, *112* (35), 13457-13462.

[37] Yang, C.; Li, M.; Zhang, W.-H.; Li, C., Controlled growth, properties, and application of CdS branched nanorod arrays on transparent conducting oxide substrate. *Solar energy materials and solar cells* **2013**, *115*, 100-107.

[38] Mort, J.; Spear, W., Hole drift mobility and lifetime in CdS crystals. *Physical Review Letters* **1962**, *8* (8), 314.

[39] Cheng, L.; Xiang, Q.; Liao, Y.; Zhang, H., CdS-based photocatalysts. *Energy & Environmental Science* **2018**, *11* (6), 1362-1391.

[40] Qin, N.; Liu, Y.; Wu, W.; Shen, L.; Chen, X.; Li, Z.; Wu, L., One-dimensional CdS/TiO<sub>2</sub> nanofiber composites as efficient visible-light-driven photocatalysts for selective organic transformation: synthesis, characterization, and performance. *Langmuir* **2015**, *31* (3), 1203-1209.

[41] Chakraborty, A. K.; Hossain, M. E.; Rhaman, M. M.; Sobahan, K., Fabrication of Bi<sub>2</sub>O<sub>3</sub>/TiO<sub>2</sub> nanocomposites and their applications to the degradation of pollutants in air and water under visible-light. *Journal of Environmental Sciences* **2014**, *26* (2), 458-465.

[42] Zou, L.; Wang, H.; Wang, X., High efficient photodegradation and photocatalytic hydrogen production of CdS/BiVO<sub>4</sub> heterostructure through Z-scheme process. *ACS Sustainable Chemistry & Engineering* **2017**, *5* (1), 303-309.

[43] Shang, F.-K.; Qi, M.-Y.; Tan, C.-L.; Tang, Z.-R.; Xu, Y.-J., Nanoscale Assembly of

CdS/BiVO<sub>4</sub> Hybrids for Coupling Selective Fine Chemical Synthesis and Hydrogen Production under Visible Light. *ACS Physical Chemistry Au* **2022**.

[44] Latif, A.; Memon, A. M.; Gadhi, T. A.; Bhurt, I. A.; Channa, N.; Mahar, R. B.; Ali, I.; Chiadò, A.; Bonelli, B., Bi<sub>2</sub>O<sub>3</sub> immobilized 3D structured clay filters for solar photocatalytic treatment of wastewater from batch to scaleup reactors. *Materials Chemistry and Physics* **2022**, *276*, 125297.

[45] Reverberi, A. P.; Varbanov, P.; Vocciante, M.; Fabiano, B., Bismuth oxide-related photocatalysts in green nanotechnology: A critical analysis. *Frontiers of Chemical Science and Engineering* **2018**, *12* (4), 878-892.

[46] Coronado-Castañeda, R.; Maya-Treviño, M.; Garza-González, E.; Peral, J.; Villanueva-Rodríguez, M.; Hernández-Ramírez, A., Photocatalytic degradation and toxicity reduction of isoniazid using β-Bi<sub>2</sub>O<sub>3</sub> in real wastewater. *Catalysis Today* **2020**, *341*, 82-89.

[47] Zhou, L.; Wang, W.; Xu, H.; Sun, S.; Shang, M., Bi<sub>2</sub>O<sub>3</sub> hierarchical nanostructures: controllable synthesis, growth mechanism, and their application in photocatalysis. *Chemistry—A European Journal* **2009**, *15* (7), 1776-1782.

[48] Raybaud, P.; Hafner, J.; Kresse, G.; Kasztelan, S.; Toulhoat, H. Structure, energetics, and electronic properties of the surface of a promoted MoS<sub>2</sub> catalyst: an ab initio local density functional study *J. Catal.* **2000**, *190* (1) 128– 143 DOI: 10.1006/jcat.1999.2743

[49] Lembke, D.; Bertolazzi, S.; Kis, A. Single-layer MoS<sub>2</sub> electronics *Acc. Chem. Res.* **2015**, *48* (1) 100– 110 DOI: 10.1021/ar500274q

[50] Radisavljevic, B.; Radenovic, A.; Brivio, J.; Giacometti, i. V.; Kis, A. Single-layer MoS<sub>2</sub> transistors *Nat. Nanotechnol.* **2011**, *6* (3) 147– 150 DOI: 10.1038/nnano.2010.279

[51] Lukowski, M. A.; Daniel, A. S.; Meng, F.; Forticaux, A.; Li, L.; Jin, S. Enhanced hydrogen evolution catalysis from chemically exfoliated metallic MoS<sub>2</sub> nanosheets *J. Am. Chem. Soc.* **2013**, *135* (28) 10274– 10277 DOI: 10.1021/ja404523s

- [52] Liu, T.; Wang, C.; Gu, X.; Gong, H.; Cheng, L.; Shi, X.; Feng, L.; Sun, B.; Liu, Z. Drug delivery with Pegylated MoS<sub>2</sub> nano-sheets for combined photothermal and chemotherapy of cancer *Adv. Mater.* **2014**, 26 (21) 3433– 3440 DOI: 10.1002/adma.201305256
- [53] Raybaud, P.; Hafner, J.; Kresse, G.; Kasztelan, S.; Toulhoat, H. Structure, energetics, and electronic properties of the surface of a promoted MoS<sub>2</sub> catalyst: an ab initio local density functional study *J. Catal.* **2000**, 190 (1) 128– 143 DOI: 10.1006/jcat.1999.2743
- [54] Xie, X.; Ao, Z.; Su, D.; Zhang, J.; Wang, G. MoS<sub>2</sub>/graphene composite anodes with enhanced performance for sodium-ion batteries: the role of the two-dimensional heterointerface *Adv. Funct. Mater.* **2015**, 25 (9) 1393– 1403 DOI: 10.1002/adfm.201404078
- [55] Shi, Z.-T.; Kang, W.; Xu, J.; Sun, Y.-W.; Jiang, M.; Ng, T.-W.; Xue, H.-T.; Yu, D. Y. W.; Zhang, W.; Lee, C.-S. Hierarchical nanotubes assembled from MoS<sub>2</sub>-carbon monolayer sandwiched superstructure nanosheets for high-performance sodium ion batteries *Nano Energy* **2016**, 22, 27– 37 DOI: 10.1016/j.nanoen.2016.02.009
- [56] Byskov, L. S.; Nørskov, J. K.; Clausen, B. S.; Topsøe, H. DFT calculations of unpromoted and promoted MoS<sub>2</sub>-based hydrodesulfurization catalysts *J. Catal.* **1999**, 187 (1) 109– 122 DOI: 10.1006/jcat.1999.2598
- [57] Takaoka, M.; Takeda, N.; Shimaoka, Y.; Fujiwara, T. Removal of mercury in flue gas by the reaction with sulfide compounds *Toxicol. Environ. Chem.* **1999**, 73 (1–2) 1– 16 DOI: 10.1080/02772249909358843
- [58] Q. Liu, X. Li, Q. He, A. Khalil, D. Liu, T. Xiang, X. Wu, L. Song  
Gram-scale aqueous synthesis of stable few-layered 1T-MoS<sub>2</sub>: Applications for visible-light-driven photocatalytic hydrogen evolution  
*Small*, 11 (2015), pp. 5556-5564
- [59] D. Late, Y.K. Huang, B. Liu, J. Acharya, S.N. Shirodkar, J. Luo, A. Yan, D. Charles, U.V. Waghmare, V.P. Dravid, C.N. Rao

Sensing behavior of atomically thin-layered MoS<sub>2</sub> transistors

ACS Nano., 7 (2013), pp. 4879-4891

[60] Y. Liu, L. Hao, W. Gao, *et al.*

Hydrogen gas sensing properties of MoS<sub>2</sub>/Si heterojunction

Sens. Actuat. B Chem., 211 (2015), pp. 537-543

[61] X. Liang, X. Zhang, W. Liu, D. Tang, B. Zhang, G. Ji

A simple hydrothermal process to grow MoS<sub>2</sub> nanosheets with excellent dielectric loss and microwave absorption performance

J. Mater. Chem. C, 4 (2016), pp. 6816-6821

[62] B. Radisavljevic, A. Radenovic, J. Brivio<sup>1</sup>, V. Giacometti, A. Kis

Single-layer MoS<sub>2</sub> transistors

Nat. Nanotech., 6 (2011), pp. 147-150

[63] K.F. Mak, C. Lee, J. Hone, J. Shan, T.F. Heinz

Atomically thin MoS<sub>2</sub>: a new direct-gap semiconductor

Phys. Rev. Lett., 105 (2010), p. 136805

[64] C. Kuru, C. Choi, A. Kargar, *et al.*

MoS<sub>2</sub> nanosheet–Pd nanoparticle composite for highly sensitive room temperature detection of hydrogen

Adv. Sci., 2 (2015), p. 1500004

[65] Järup, L.J.B.m.b., Hazards of heavy metal contamination. 2003. 68(1): p. 167-182.

[66] Zawierucha, I., et al., Immobilized materials for removal of toxic metal ions from surface/groundwaters and aqueous waste streams. 2016. 18(4): p. 429-444.

[67] O. Xu, Q., Zhang, L., Yu, J., Wageh, S., Al-Ghamdi, A.A., and Jaroniec, M. (2018).

Direct Z-scheme photocatalysts: principles, synthesis, and applications. Mater. Today 21, 1042–1063.

- [68] Mei, F., Dai, K., Zhang, J., Li, W., and Liang, C. (2019). Construction of Ag SPR-promoted step-scheme porous g-C<sub>3</sub>N<sub>4</sub>/Ag<sub>3</sub>VO<sub>4</sub> heterojunction for improving photocatalytic activity. *Appl. Surf. Sci.* 488, 151–160.
- [69]. Jia, X., Han, Q., Zheng, M., and Bi, H. (2019). One pot milling route to fabricate step-scheme Ag<sub>2</sub>O/BiOAc photocatalyst: energy band structure optimized by the formation of solid solution. *Appl. Surf. Sci.* 489, 409–419.
- [70]. Wang, J., Zhang, Q., Deng, F., Luo, X., and Dionysiou, D.D. (2020). Rapid toxicity elimination of organic pollutants by the photocatalysis of environment-friendly and magnetically recoverable step-scheme SnFe<sub>2</sub>O<sub>4</sub>/ZnFe<sub>2</sub>O<sub>4</sub> nano-heterojunctions. *Chem. Eng. J.* 379, 122264.
- [71]. Xu, Q., Ma, D., Yang, S., Tian, Z., Cheng, B., and Fan, J. (2019). Novel g-C<sub>3</sub>N<sub>4</sub>/g-C<sub>3</sub>N<sub>4</sub> S-scheme isotype heterojunction for improved photocatalytic hydrogen generation. *Appl. Surf. Sci.* 495, 143555.
- [72] He, F., Meng, A., Cheng, B., Ho, W., and Yu, J. (2020). Enhanced photocatalytic H<sub>2</sub>-production activity of WO<sub>3</sub>/TiO<sub>2</sub> step-scheme heterojunction by graphene modification. *Chin. J. Catal.* 41, 9–20.
- [73] 69. Mu, J., Teng, F., Miao, H., Wang, Y., and Hu, X. (2020). In-situ oxidation fabrication of 0D/2D SnO<sub>2</sub>/SnS<sub>2</sub> novel Step-scheme heterojunctions with enhanced photoelectrochemical activity for water splitting. *Appl. Surf. Sci.* 501, 143974.
- [74]. Wang, R., Shen, J., Zhang, W., Liu, Q., Zhang, M., Zulfiqar, H.T., and Tang, H. (2020). Build-in electric field induced step-scheme TiO<sub>2</sub>/W<sub>18</sub>O<sub>49</sub> heterojunction for enhanced photocatalytic activity under visible-light irradiation. *Ceram. Int.* 46, 23–30.
- [75]. Hu, T., Dai, K., Zhang, J., Zhu, G., and Liang, C. (2019). One-pot synthesis of step-scheme Bi<sub>2</sub>S<sub>3</sub>/porous g-C<sub>3</sub>N<sub>4</sub> heterostructure for enhanced photocatalytic performance. *Mater. Lett.* 257, 126740.

- [76] S. Banerjee, S. C. Pillai, P. Falaras, K. E. O'shea, J. A. Byrne, and D. D. Dionysiou, "New insights into the mechanism of visible light photocatalysis," *The journal of physical chemistry letters*, vol. 5, pp. 2543-2554, 2014.
- [77] S. P. Sajjadi, "Sol-gel process and its application in Nanotechnology," *J. Polym. Eng. Technol*, vol. 13, pp. 38-41, 2005.
- [78] Walock, M., Nanocomposite coatings based on quaternary metal-nitrogen and nanocarbon systems. 2012.
- [79] Das, H., Characterization of defects and evaluation of material quality of low temperature epitaxial growth. 2010.
- [80] F. Chen, R. Zhou, L. Yang, M. Shi, G. Wu, M. Wang and H. Chen, *J. Phys. Chem. C*, 2008, 112, 13457.
- [81] C. Yang, M. Li, W. H. Zhang and C. Li, *Sol. Energy Mater. Sol. Cells*, 2013, 115, 100.
- [82] H. Zhang, D. Yang and X. Ma, *Mater. Lett.*, 2007, 61, 3507.
- [83] Y. Huang, F. Sun, T. Wu, Q. Wu, Z. Huang, H. Su and Z. Zhang, *J. Solid State Chem.*, 2011, 184, 644.
- [84] J. Mort and W. E. Spear, *Phys. Rev. Lett.*, 1962, 8, 314.
- [85] L. Zhang, X. Fu, S. Meng, X. Jiang, J. Wang and S. Chen, *J. Mater. Chem. A*, 2015, 3, 23732
- [86] Q. Li , B. D. Guo , J. G. Yu , J. R. Ran , B. H. Zhang , H. J. Yan , J. R. Gong , *J. Am. Chem. Soc.* 2011 , 133 , 10878 .
- [87] G. Prieto, H. Tüysüz, N. Duyckaerts, J. Knossalla, G.-H. Wang, F. Schüth
- [88] G., Tüysüz, H., Duyckaerts, N., Knossalla, J., Wang, G. H., & Schüth, F. (2016). Hollow nano-and microstructures as catalysts. *Chemical reviews*, 116(22), 14056-14119.
- [89] Deng, Z., Chen, M., Gu, G., & Wu, L. (2008). A facile method to fabricate ZnO hollow spheres and their photocatalytic property. *The journal of physical chemistry B*, 112(1), 16-22

- [90] Lu, W., Gao, S., & Wang, J. (2008). One-pot synthesis of Ag/ZnO self-assembled 3D hollow microspheres with enhanced photocatalytic performance. *The Journal of Physical Chemistry C*, 112(43), 16792-16800.
- [91] Luo, Q. P., Yu, X. Y., Lei, B. X., Chen, H. Y., Kuang, D. B., & Su, C. Y. (2012). Reduced graphene oxide-hierarchical ZnO hollow sphere composites with enhanced photocurrent and photocatalytic activity. *The Journal of Physical Chemistry C*, 116(14), 8111-8117.
- [92] H Aboud, K., MH AL-Jawad, S., & Jamal Imran, N. (2022). Preparation and Characterization of Hierarchical CdS Nanoflowers for Efficient Photocatalytic Degradation. *Journal of Nanostructures*, 12(2), 316-329.
- [93] Xu, Y., Zhao, W., Xu, R., Shi, Y., & Zhang, B. (2013). Synthesis of ultrathin CdS nanosheets as efficient visible-light-driven water splitting photocatalysts for hydrogen evolution. *Chemical communications*, 49(84), 9803-9805.
- [94] Mahdi, M. A., Hassan, J. J., Ng, S. S., & Hassan, Z. (2012). Growth of CdS nanosheets and nanowires through the solvothermal method. *Journal of crystal growth*, 359, 43-48.
- [95] Chen, R., Shen, Z. R., Wang, H., Zhou, H. J., Liu, Y. P., Ding, D. T., & Chen, T. H. (2011). Fabrication of mesh-like bismuth oxide single crystalline nanoflakes and their visible light photocatalytic activity. *Journal of Alloys and Compounds*, 509(5), 2588-2596.
- [96] Huang, Y., Qin, J., Liu, X., Wei, D., & Seo, H. J. (2019). Hydrothermal synthesis of flower-like Na-doped  $\alpha$ -Bi<sub>2</sub>O<sub>3</sub> and improved photocatalytic activity via the induced oxygen vacancies. *Journal of the Taiwan Institute of Chemical Engineers*, 96, 353-360.
- [97] Sudapalli, A. M., & Shimpi, N. G. (2022). Hierarchical self-assembly of 0D/2D  $\beta$ -Bi<sub>2</sub>O<sub>3</sub> crossandra flower morphology exhibits excellent photocatalytic activity against bromophenol dyes. *Optical Materials*, 132, 112849.
- [98] Tang, G., Wang, Y., Chen, W., Tang, H., & Li, C. (2013). Hydrothermal synthesis and

- characterization of novel flowerlike MoS<sub>2</sub> hollow microspheres. *Materials Letters*, 100, 15-18
- [99] Li, W. J., Shi, E. W., Ko, J. M., Chen, Z. Z., Ogino, H., & Fukuda, T. (2003). Hydrothermal synthesis of MoS<sub>2</sub> nanowires. *Journal of Crystal Growth*, 250(3-4), 418-422.
- [100] Zelenski, C. M., & Dorhout, P. K. (1998). Template synthesis of near-monodisperse 1 microscale nanofibers and nanotubules of MoS<sub>2</sub>. *Journal of the American Chemical Society*, 120(4), 734-742
- [101] Weber, T., Muijsers, J. C., Van Wolput, J. H. M. C., Verhagen, C. P. J., & Niemantsverdriet, J. W. (1996). Basic reaction steps in the sulfidation of crystalline MoO<sub>3</sub> to MoS<sub>2</sub>, as studied by X-ray photoelectron and infrared emission spectroscopy. *The Journal of Physical Chemistry*, 100(33), 14144-14150.
- [102] Fu, P., et al., Thermal stability and microstructure characterization of MgAl<sub>2</sub>O<sub>4</sub> nanoparticles synthesized by reverse microemulsion method. *Materials Research*, 2013. 16(4): p. 844-849.
- [103] Fadley, C. S. (2010). X-ray photoelectron spectroscopy: Progress and perspectives. *Journal of Electron Spectroscopy and Related Phenomena*, 178, 2-32.
- [104] Gohain, N., Studies on the structure and function of phenazine modifying enzymes PhzM and PhzS involved in the biosynthesis of pyocyanin. 2009
- [105] Fadley, C. S. (2010). X-ray photoelectron spectroscopy: Progress and perspectives. *Journal of Electron Spectroscopy and Related Phenomena*, 178, 2-32.



